





Localization and spectral structure in two-dimensional quasicrystal potentialsZhaoxuan Zhu , Shengjie Yu, Dean Johnstone , and Laurent Sanchez-Palencia 
CPHT, CNRS, Ecole Polytechnique, IP Paris, F-91128 Palaiseau, France (Received 19 July 2023; revised 26 November 2023; accepted 20 December 2023; published 17 January 2024)

Quasicrystals, a fascinating class of materials with long-range but nonperiodic order, have revolutionized our understanding of solid-state physics due to their unique properties at the crossroads of long-range-ordered and disordered systems. Since their discovery, they continue to spark broad interest for their structural and electronic properties. The quantum simulation of quasicrystals in synthetic quantum matter systems offers a unique playground to investigate these systems with unprecedented control parameters. Here, we investigate the localization properties and spectral structure of quantum particles in two-dimensional quasicrystalline optical potentials. While states are generally localized at low energy and extended at high energy, we find alternating localized and critical states at intermediate energies. Moreover, we identify a complex succession of gaps in the energy spectrum. We show that the most prominent gap arises from strongly localized ring states, with the gap width determined by the energy splitting between states with different quantized winding numbers. In addition, we find that these gaps are stable for quasicrystals with different rotational symmetries and potential depths, provided that other localized states do not enter the gap generated by the ring states. Our findings shed light on the unique properties of quantum quasicrystals and have implications for their many-body counterparts.

DOI: [10.1103/PhysRevA.109.013314](https://doi.org/10.1103/PhysRevA.109.013314)**I. INTRODUCTION**

The discovery of quasicrystals in the early 1980s [1] marked a paradigm shift in crystallography and solid-state physics, prompting investigations into their structural and electronic properties [2–7]. Quasicrystals are usually synthesized in the laboratory after fast solidification of certain alloys [1,8], but have also been observed at their natural state in meteorites [9,10] and residues of nuclear blasts [11]. Unlike conventional crystal solids, quasicrystals lack translational invariance, but retain long-range order, hence challenging the traditional notions of crystalline order [12,13]. According to the crystallographic restriction theorem, periodic crystals can only possess twofold, threefold, fourfold, or sixfold rotational symmetries [14,15]. Quasicrystals, however, show discrete rotation symmetries of orders $n = 5, 7, 8, 9, \dots$, hence incompatible with periodic long-range order [16]. This is evidenced by Bragg spectroscopy patterns with clear diffraction peaks arranged in accordance to the forbidden rotational symmetries [17,18]. The key feature of quasicrystals is then their quasiperiodicity, which amounts to the fact that finite patterns can be approximately reproduced at arbitrary long distances, but usually not exactly and not periodically. This crystallographic definition is now pivotal in identifying and classifying quasicrystals. Due to their structure, quasicrystals can also possess distinct electronic properties that set them apart from standard materials. The electronic behavior in quasicrystals is governed by complex wave interference patterns, which can, for instance, give rise to phason quasiparticles [19–21], exotic transport properties [22–26], and an intricate energy spectrum [27–29]. Understanding these distinctive electronic properties is vital for unraveling the underlying mechanisms governing quasicrystals and their potential applications.

Recent developments in quantum simulation offers a unique playground to study the physics of complex quantum systems in controlled environments, with the promise of shedding light on their fundamental properties [30–33]. In recent years, considerable progress has been made in the quantum simulation of quasicrystals, leveraging various experimental platforms, including photonic crystals [34–37], quantum fluids of light [38–40], and ultracold quantum gases [41,42]. Notably, the use of ultracold atoms as quantum simulators has gained prominence, owing to the unprecedented control over experimental parameters [43–48]. While one-dimensional (1D) quasiperiodic systems have been extensively studied in the last two decades [49–67], much attention is now devoted to quasicrystals in dimensions higher than one [42,68–75]. Previous studies on two-dimensional (2D) optical quasicrystals have focused on investigating the emergence of long-range quasicrystalline order using matter-wave interferometry [41,42], single-particle Anderson-type localization [41,68,69], as well as Bose glass physics in weakly interacting [69–71,76] and strongly correlated Bose gases [72–74]. In this respect, the physics of single quantum particles in a quasicrystal potential plays a central role, not only for their unique properties but also for understanding the many-body problem. On the one hand, detailed studies of a variety of 1D quasiperiodic systems have revealed exotic localization and fractal properties, which clearly distinguishes generic quasiperiodic systems from disordered ones. Even richer behavior may be expected for 2D quasicrystalline systems, and a detailed study of the specific configurations implemented on current experimental platforms is deserved. On the other hand, understanding the single-body problem is decisive for understanding the many-body properties, especially in regards to the competition of localization and interparticle interactions, which governs quantum phase diagrams. For

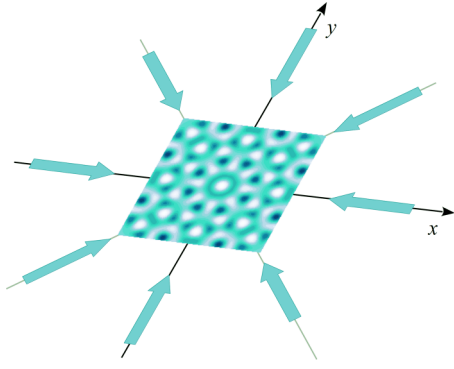


FIG. 1. Optical quasicrystal for ultracold atoms. A 2D quasicrystal potential with eightfold rotation symmetry is realized using four pairs of counterpropagating laser beams, making successive angles of 45° each.

instance, it has been recently shown that the emergence of a Bose glass and an insulating Mott phase in strongly correlated Bose gases subjected to shallow quasicrystal potentials can be related to localization and spectral gaps of noninteracting systems [74].

In this work, we investigate the localization properties and the structure of the energy spectrum for noninteracting quantum particles in two-dimensional quasicrystal potentials, as realized for ultracold-atom quantum simulators. While quantum states are generally localized at low energies and extended at high energies, we find an alternation of localized and critical states at intermediate energies. Finite-size scaling analysis of the inverse participation ratio unveils a power-law scaling, with a noninteger fractal dimension, for systems up to sizes of several hundreds of the natural length scale (optical wavelength). Furthermore, the energy spectrum shows a complex succession of bands and gaps, and we show that the most prominent gap is generated by localized ring states, and the gap width is controlled by the energy splitting between states with different quantized winding numbers.

We present our results as follows. A 2D optical quasicrystal with eightfold rotational symmetry is first introduced in Sec. II and we provide a general overview of the localization and spectral properties in Sec. III. The localization properties are then discussed in greater detail within Sec. IV, including the structure of localized, critical, and extended states, and their identification from a finite-size scaling analysis of the inverse participation ratio. Next, in Sec. V, we investigate the formation of gaps in the energy spectrum and show that they originate from localized ring states with different winding numbers. Finally, in Sec. VI, we extend this discussion to quasicrystal potentials with other discrete rotational symmetries, before ending with our conclusions and the implications of our results in Sec. VII.

II. QUASICRYSTAL POTENTIAL

The quasicrystal potential we consider, except whenever mentioned, is the sum of four one-dimensional standing waves with amplitude V_0 and lattice period $a = \pi/|\mathbf{G}_k|$, and successively rotated by an angle of 45° (see Fig. 1). It can be

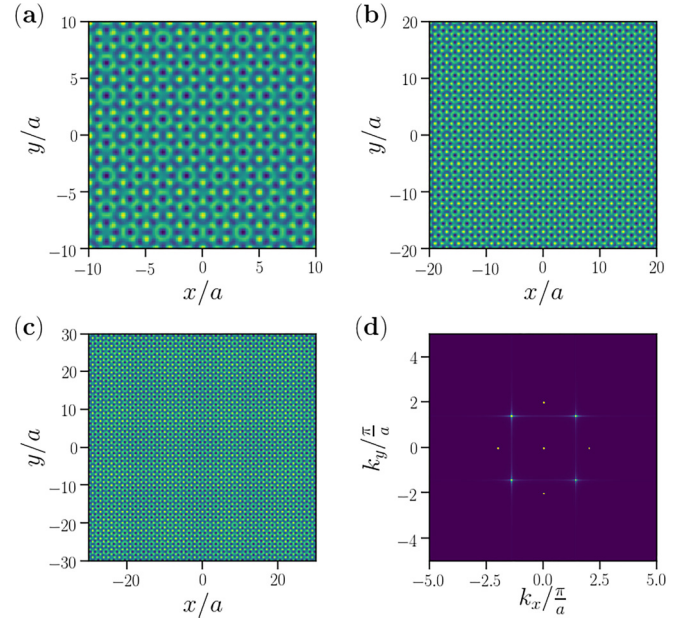


FIG. 2. Eightfold quasicrystal potential. (a)–(c) Real-space potential, Eq. (1), with $\phi_k = 0$ for all k , plotted at various scales, for the linear system sizes (a) $L = 20a$, (b) $L = 40a$, and (c) $L = 60a$, all centered at $\mathbf{r} = 0$. (d) Fourier transform of the potential. The color scale represents the value of the potential or its Fourier transform from low values (dark colors) to high values (light colors).

written as

$$V(\mathbf{r}) = V_0 \sum_{k=1}^4 \cos^2(\mathbf{G}_k \cdot \mathbf{r} + \phi_k), \quad (1)$$

with $\mathbf{G}_1 = \frac{\pi}{a}(1, 0)$, $\mathbf{G}_2 = \frac{\pi}{a}(\frac{1}{\sqrt{2}}, \frac{1}{\sqrt{2}})$, $\mathbf{G}_3 = \frac{\pi}{a}(0, 1)$, $\mathbf{G}_4 = \frac{\pi}{a}(-\frac{1}{\sqrt{2}}, \frac{1}{\sqrt{2}})$, position vectors $\mathbf{r} = (x, y)$, and phase factors ϕ_k of laser beam k . This potential can be realized in ultracold-atom experiments using four retroreflected laser beams with slightly shifted frequencies to suppress mutual coherence [42,69,76]. Generalizations to quasicrystal potentials with higher rotational symmetries are discussed in Sec. VI.

The eightfold quasicrystal potential with all $\phi_k = 0$ is shown at different length scales on Figs. 2(a)–2(c), which shows the quasirepetition of short-range structures. Here, we can observe the underlying eightfold rotational symmetry, which is incompatible with periodic order. This is better seen in Fig. 2(d), which shows the Fourier transform of the 2D potential, Eq. (1). The discreteness of the Fourier pattern is a characteristic of long-range order, while the eight spots regularly arranged on a circle of radius $|k| = 2\pi/a$ directly reflect the eightfold discrete rotational symmetry and absence of periodic order. For $\phi_k = 0$, the origin of the 2D system at $\mathbf{r} = 0$ is a rotational symmetry center. The spot at $k_x = k_y = 0$ is due to the finite average value of the potential, $\int \frac{d^2\mathbf{r}}{L^2} V(\mathbf{r}) = 2V_0$, where L is the linear system size. It may be canceled out by shifting the potential by $-2V_0$.

To avoid exact rotation symmetry around the center at $(x, y) = (0, 0)$, for the majority of our results, we consider an off-centered square area, which is more generic. For instance, it lifts exact degeneracies of strongly localized states around

potential minima, that are, however, very far apart from each other. This facilitates the discrimination of localized and extended states. In practice, we shift the center from $(x, y) = (0, 0)$ to $(x_0, y_0) = (-13543a, 196419a)$, which is far beyond the system borders we consider. This is equivalent to phase shifts of the laser beams with $\phi_1 = 0$, $\phi_2 \simeq 0.8597\pi$, $\phi_3 = \pi$, and $\phi_4 \simeq 1.5540\pi$. Note that the direction of the symmetry center to the system center is $\theta = \arctan(y_0/x_0) \simeq -86.06^\circ$. It is away from any special directions associated with the discrete rotation symmetry, which are multiples of 22.5° .

III. SINGLE-PARTICLE SPECTRUM

We now consider massive quantum particles in the quasicrystal potential of Eq. (1). The single-particle Hamiltonian is

$$H = \frac{\mathbf{p}^2}{2M} + V(\mathbf{r}), \quad (2)$$

where $\mathbf{p} = -i\hbar\nabla$ is the 2D momentum operator and M is the particle mass. The eigenstates of this Hamiltonian are obtained using exact numerical diagonalization. In practice, the diagonalizations are performed in square areas of linear sizes L . We use the lattice constant a as the length unit and the recoil energy $E_r = \pi^2\hbar^2/2Ma^2$ as the energy unit. We use the spatial discretization $dx = 0.1a$ and the typical system size is $L = 60a$, except whenever mentioned. Due to the finite discretization, only the lowest-energy eigenstates are retained. They correspond to those whose variation scale λ significantly exceeds the discretization dx . For an eigenstate with energy E , the typical de Broglie wavelength is $\lambda = \frac{2\pi\hbar}{\sqrt{2ME}}$, which yields the restriction on the eigenenergy as $E/E_r \ll \frac{4}{(dx/a)^2} = 400$. In practice, we consider potential amplitudes up to $V_0 = 10E_r$ and we keep the eigenstates up to energy $E = 8V_0$.

In the numerics, we must impose boundary conditions. Owing to the nonperiodicity of the potential, any choice would distort the wave functions in the vicinity of the edges, and some care should be taken over the states obtained in finite squares. We should indeed keep the states that faithfully represent the spectrum in the thermodynamic limit, and discard the states that are created by boundary effects. Here, we choose periodic boundary conditions, where nonphysical edge states may appear in the vicinity of the system boundaries. We have checked that such edge states disappear from their initial location when we repeat the diagonalization in a larger system, while new edge states appear near the new boundaries, confirming that they are indeed created by the boundaries. To get a spectrum representative of the thermodynamic limit, these edge states are thus excluded as follows: We first reduce each wave function to a binary map. If the wave-function magnitude at a certain position is larger than 10% of the maximum of the wave-function magnitude, it maps to 1; otherwise it maps to 0. Then, at each point with value 1, we compute the quantity $Z = 1 - 2d/L$, where d is the distance to the nearest edge, as well as, for each eigenstate, its average \bar{Z} . The criterion used in this work to only keep bulk states is the combination of the following two: (i) $\bar{Z} < 0.9$ and (ii) the position of the wave-function maximum is at a distance larger than $3a$ from the nearest edge of the system. If an eigenstate fulfills both conditions, it is identified as a

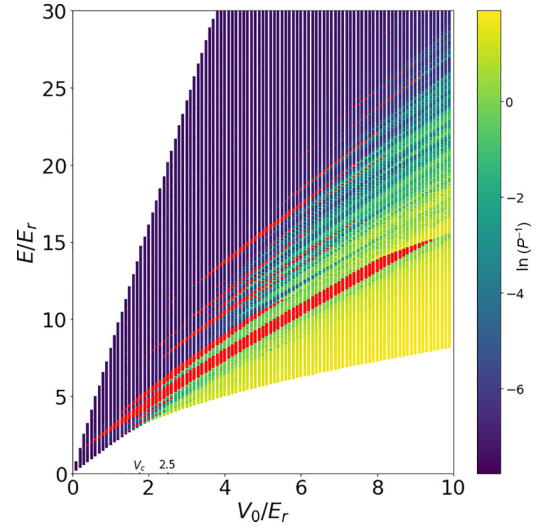


FIG. 3. Energy spectrum of the quasicrystal potential for various V_0 . The system size is $L = 60a$, centered at $(x_0, y_0) = (-13543a, 196419a)$. We keep the eigenstates with energy up to $8V_0$ for potential amplitude $V_0 \lesssim 4E_r$ and up to $30E_r$ for larger potential V_0 . The color scale shows the value of $\ln(P^{-1})$ for each eigenstate, while the gaps are colored red.

legitimate bulk state; otherwise, it is identified as an edge state and is excluded.

Figure 3 shows the single-particle spectrum of the Hamiltonian versus the quasicrystal amplitude V_0 and the eigenenergy E , up to $8E_r$ [the color scale represents the IPR of each eigenstate (see Sec. IV)]. The spectrum has a rich structure and shows a series of energy gaps (highlighted in red), each in specific ranges of the quasicrystal amplitude. The largest gap has been identified earlier [74,75], while the smallest is more elusive. To locate these gaps systematically, we apply the following method for each spectrum corresponding to different values of V_0 : For each set of successive 500 eigenstates, we calculate all the eigenenergy differences between neighboring bulk states and then take the average value of all these eigenenergy differences. If any eigenenergy difference is larger than 50 times that mean value, it is identified as a gap. Otherwise, it is considered to be in an energy band. We have checked that the gaps thus identified for a system of linear size $L = 60a$ agree with another approach where the energy resolution is fixed, and are stable against increasing system sizes (see Appendix A).

IV. LOCALIZATION PROPERTIES

Quasiperiodic systems are known to exhibit localization of eigenstates [60,77–81]. To study these properties, we compute, for each single-particle eigenstate, the inverse participation ratio (IPR)

$$P^{-1} = \frac{\int d\mathbf{r} |\psi(\mathbf{r})|^4}{(\int d\mathbf{r} |\psi(\mathbf{r})|^2)^2}, \quad (3)$$

where $\psi(\mathbf{r})$ is the 2D eigenstate wave function and P^{-1} represents the IPR. Generally, in sufficiently large systems, states with large IPR are localized while states with small

IPR are delocalized, which may be either extended or critical. Figure 3 shows, for every eigenstate, $\ln(P^{-1})$ versus V_0 and E in color scale. For small quasicrystal amplitude V_0 , all the eigenstates appear delocalized. This is consistent with the critical potential for localization $V_c \simeq 1.76E_r$, found in previous works [68,72]. As V_0 increases, the low-energy eigenstates tend to localize since long-range coherence is suppressed as the quasicrystal becomes deeper, while higher-energy eigenstates remain delocalized. In the intermediate-energy range, the localization behavior is richer. We find that eigenstates with large and small IPR coexist and, in particular, the IPR is nonmonotonous against energy.

A. Finite-size scaling analysis

To study localization in more detail, the bare value of the IPR is insufficient and we consider a more rigorous characterization of localization. It is provided by the scaling of IPR with the system size L , $P^{-1} \sim L^\gamma$. In 2D, localized states are characterized by $\gamma = 0$ and extended states by $\gamma = -2$. Any intermediate value of γ between 0 and -2 then identifies a critical state [80,81]. In the following, we focus on the case $V_0 = 2.5E_r$, which is larger than the critical potential $V_c \simeq 1.76E_r$, but similar results are found for other amplitudes of the quasicrystal potential.

Studying the finite-size scaling properties of the IPR requires comparing eigenstates for different sizes. However, diagonalization in systems with different sizes gives different total numbers of eigenstates, as the density of states generally scales with the system area. Hence, given an eigenstate for a certain system size, there is always some arbitrariness on picking up the corresponding eigenstate for another system size to be compared with. To overcome this issue, we compute the averaged IPR of all eigenstates in a narrow energy window, $\overline{P^{-1}}$. The width of the energy window is chosen to be $\delta E = 0.01E_r$, narrow enough such that the eigenstates in the energy window have similar localization properties, but large enough to have enough states to average. Then, the scaling exponent γ considered below refers to this averaged $\overline{P^{-1}}$, and characterizes the localization properties in the corresponding energy window.

For instance, Fig. 4 shows the scaling of the P^{-1} versus the system size from $L = 20a$ to $300a$, for three different energy windows. In all cases, it shows a clear power-law scaling, $\text{IPR} \sim L^\gamma$, and the exponent γ is found by a linear fit of $\ln(\overline{P^{-1}})$ versus $\ln(L/a)$. Figure 4(a1) corresponds to energy $E \simeq 4E_r$. The quantity $\ln(\overline{P^{-1}})$ fluctuates with the system size but shows no clear increasing or decreasing tendency. Linear regression of the data points yields the slope $\gamma = -0.04 \pm 0.03$. The small value of $|\gamma|$ indicates that the states in this energy window are localized. An example of the wave function of an eigenstate in this energy window is plotted in Fig. 4(b1). The state is localized in a few local potential wells, consistently with strong localization. Figure 4(a2) corresponds to energy $E \simeq 6.45E_r$. In this case, linear regression yields the slope $\gamma = -2.06 \pm 0.06$, corresponding to an extended state. The wave function of an eigenstate in this energy window, shown in Fig. 4(b2), consistently covers the full system area, although not homogeneously. Finally, Fig. 4(a3) corresponds to energy $E \simeq 5.81E_r$. It also shows a clear linear behavior in

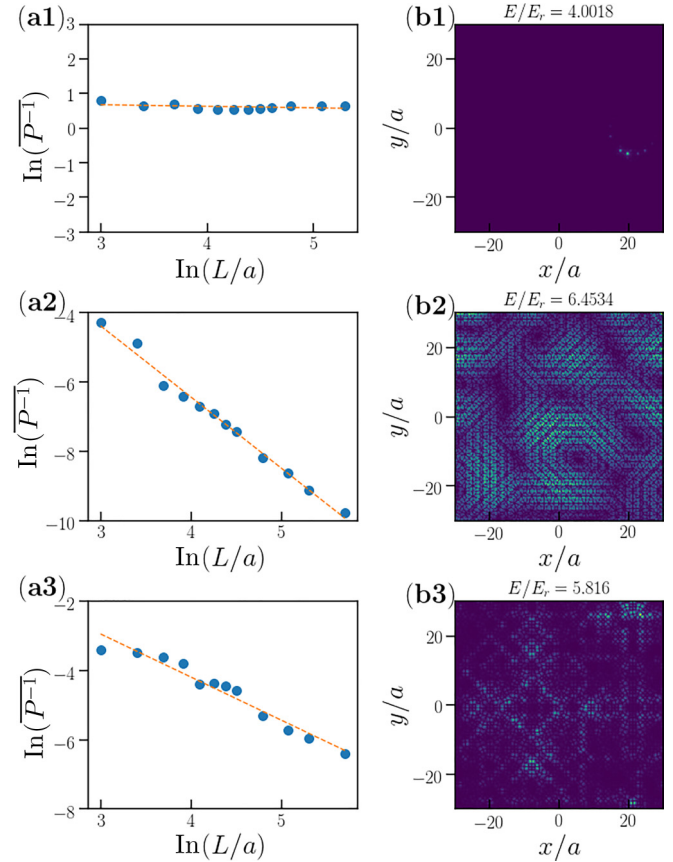


FIG. 4. Localization properties of some eigenstates. The left column (a) shows $\ln(\overline{P^{-1}})$ versus $\ln(L/a)$ for all eigenstates in various energy windows. Blue disks are data points while orange dashed lines show linear fits. The quasicrystal amplitude is $V_0 = 2.5E_r$ and the system sizes for linear regressions range from $L = 20a$ to $300a$. (a1) The energy window is $E/E_r \in [4.00, 4.01]$ and the linear fit yields $\gamma = -0.04 \pm 0.03$. (a2) The energy window is $E/E_r \in [6.45, 6.46]$ and the linear fit yields $\gamma = -2.06 \pm 0.06$. (a3) The energy window is $E/E_r \in [5.81, 5.82]$ and the linear fit yields $\gamma = -1.25 \pm 0.09$. The right column (b) shows examples of eigenstates in the corresponding energy windows, with energies indicated on the top of each panel. The wave functions plotted here are computed for the system size $L = 60a$.

log-log scale and the slope is found to be $\gamma = -1.25 \pm 0.09$, significantly far from both 0 or -2 . In this energy window, the states are thus neither localized nor extended, i.e., they are critical. A typical eigenstate is plotted in Fig. 4(b3). Unlike localized states, these critical states extend over the full system but, compared to extended states, they only cover a limited proportion of the area. Note, in general, γ may exhibit quite large standard deviations, particularly when one considers domains where critical states appear. In our calculations, we consider the average value and standard deviation from the linear fit, and do not take into account the spread of individual IPR values. As we discuss in Appendix B, the distribution of the IPR for localized and extended states is rather narrow, and does not contribute significant errors. In contrast, for critical states, we tend to observe a broader distribution of coefficients γ even in rather narrow energy windows, which, however, remains clearly distinct from either localized or extended states. This

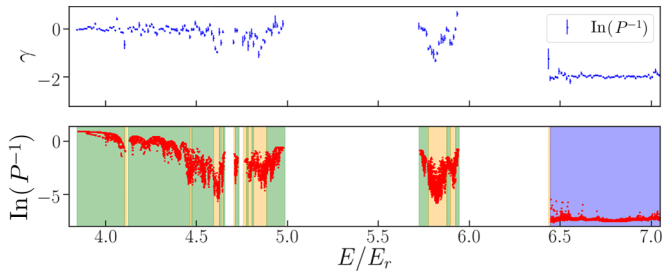


FIG. 5. Localization spectrum in the quasicrystal potential. Upper row: scaling exponent γ of the $P^{-1} \sim L^\gamma$ for system sizes ranging from $L = 20a$ to $100a$, except in some narrow energy windows where data for larger sizes, $L = 120a, 160a, 200a, 300a$, are also calculated. Lower row: classification of different kinds of states. The values of $\ln(P^{-1})$ for all eigenstates with system size $L = 80a$ are plotted versus their eigenenergies. Localization properties are shown as background colors: green for localized states, blue for extended states, and orange for critical states. The potential amplitude is $V_0 = 2.5E_r$.

behavior is strongly indicative of a critical regime, despite the significant spread of IPR values (and hence larger error in γ). The value of γ should therefore be read as a qualitative figure within critical domains, rather than a quantitative one.

Systematic finite-size scaling and linear fits are performed over the full spectrum, with results shown in Fig. 5.

For details, see Appendix B. Generally, the system sizes range from $L = 20a$ to $100a$. For some energy windows, notably where critical states appear, we use larger sizes, up to $L = 300a$, so as to check that the scaling behavior of the IPR persists for larger system sizes. The exponent γ found from linear fits of $\ln(P^{-1})$ versus $\ln(L/a)$ is shown in the upper row of Fig. 5. The results show that the lowest-energy states are localized, with $\gamma \simeq 0$. For energy $E \gtrsim 6.45E_r$, i.e., above the second large energy gap, all states are extended, with $\gamma \simeq -2$. In the intermediate energy range, there are critical states whose scaling exponent γ is neither 0 nor -2 but clearly in-between. Taking into account the uncertainty of the fitted exponents γ , energy ranges with different kinds of localization properties can be identified as follows, with results shown in the lower row of Fig. 5: Localized states for $\gamma > -0.25$ (green), extended states for $\gamma < -1.75$ (blue), and critical states for $-1.75 < \gamma < -0.25$ (yellow). Also shown is $\ln(P^{-1})$ for each eigenstate calculated for $L = 80a$ (red dots). The behavior of the DOS shows that there are a significant number of states of each kind in the spectrum. The behavior of $\ln(P^{-1})$ is rather smooth, up to significant fluctuations. Interestingly, we find that critical and localized states can coexist at intermediate energies, with no clear mobility edge or separation between localized and critical domains. This is reminiscent of “anomalous mobility edges” separating bands of localized states and bands of critical states as found in other quasiperiodic models [67].

General properties of localized, extended, and critical states are further discussed in the following subsections.

B. Localized states

Localized states generally appear in the low-energy range, as well as at some energy band edges, nearby energy gaps (see

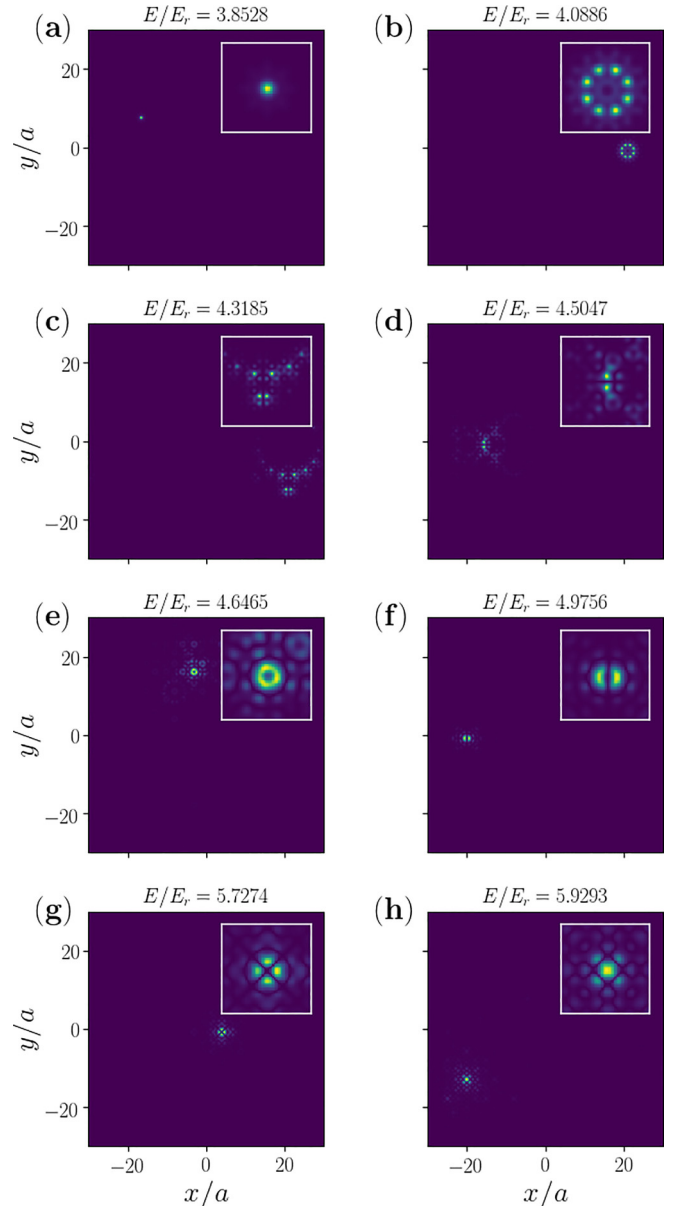


FIG. 6. Wave functions of typical localized states in various energy ranges. The eigenenergy, indicated on the top of each panel, increases in the reading order, from (a) to (h). The quasicrystal potential amplitude is $V_0 = 2.5E_r$, and the system size is $L = 60a$. The insets show magnifications of the corresponding panel in the vicinity of the localization center.

Fig. 5). Typical localized states in different energy ranges are plotted on Fig. 6, with eigenenergy increasing in the reader order, from Figs. 6(a)–6(h). The insets show magnification of the main panel in the vicinity of the localization center. The states with lowest energies are strongly localized in a single local potential well [see Fig. 6(a)]. As the energy increases, the states start to cover a few potential wells. Some states are localized in regions where the local potential is almost eightfold rotational symmetric, and the eigenstates form rings composed of eight almost equivalent spots [see Fig. 6(b)]. Similar ring states exist with 16 spots (not shown). Other localized states cover a small cluster of different potential

wells, such that the tunneling between them is large enough to compensate the eigenenergy differences between the local potential wells [see Figs. 6(c) and 6(d)]. As the energy further increases, states composed of one or many small rings begin to appear. Figure 6(e) shows such a localized state with one small ring, with eigenenergy slightly below the energy gap at $E \simeq 4.65E_r$. The small ring actually corresponds to a set of several local shallow potential wells that are very near by each other, and the wave function on these wells merges into an almost homogeneous circle. Figures 6(f) and 6(g) are localized states with energies, respectively, right below and right above the first large energy gap in, approximately, $E/E_r \in [5, 5.7]$. They are also states located on small rings of nearby potential wells, as for Fig. 6(e). However, unlike in Fig. 6(e), these small-ring wave functions have, respectively, one or two node lines due to different phase winding numbers. These states play special roles in the spectral structure and will be further discussed in Sec. V. Localized states with relatively high energies do not all have similar ring structures. Some of these states are localized in one or multiple potential wells, as in Fig. 6(h).

C. Extended states

States with high enough eigenenergies are all extended (see Fig. 5). For a potential amplitude $V_0 = 2.5E_r$, extended states appear after the second large gap, i.e., for energy $E \gtrsim 6.45E_r$. Typical extended states are plotted on Fig. 7. They cover the full system area quasihomogeneously, even though some dark node regions due to large scale modulation of the wave function may appear, as for instance in Fig. 7(a3). Extended wave functions contain many spots separated by node lines. For low-enough energy, each island has a size comparable with the lattice constant a , and forms a rather ordered pattern [see Fig. 7(a3)]. For states with higher energy, the wave-function variations become stronger and the typical size of the islands gets smaller. It goes down to the de Broglie wavelength $\lambda = 2\pi\hbar/\sqrt{2mE}$ of the quasi-plane waves rather than the potential profile. Correspondingly, the states show a complex, quite disordered, pattern determined by multiple scattering on the quasicrystal potential [see Figs. 7(a1) and 7(a2)].

While the IPR alone does not seem to characterize the crossover from “ordered” extended states to “disordered” ones, a better understanding can be gained by looking at the density profiles in momentum space, as shown in Figs. 7(b1)–7(b3). Consider first the highest-energy states [Figs. 7(b1) and 7(b2)]. The momentum distribution of such states is concentrated around a marked circle, with a smaller spreading when the energy increases. This structure may be understood using simple perturbation theory: Extended states with high-enough energy E are constructed from plane waves with momentum k_E such that $E = \hbar^2 k_E^2/2M + \langle V \rangle$, where $\langle V \rangle \simeq 2V_0$ is the potential-energy contribution for purely plane waves. We consistently find that the circle with radius k_E [shown in red in Figs. 7(b1)–7(b3)] coincides with the dominant momentum components of the extended wave function. The quasicrystal potential weakly couples many plane waves with a modulus of the momentum nearly equal to k_E in almost all directions and within a structure consistent with the quasicrystalline eightfold rotational symmetry.

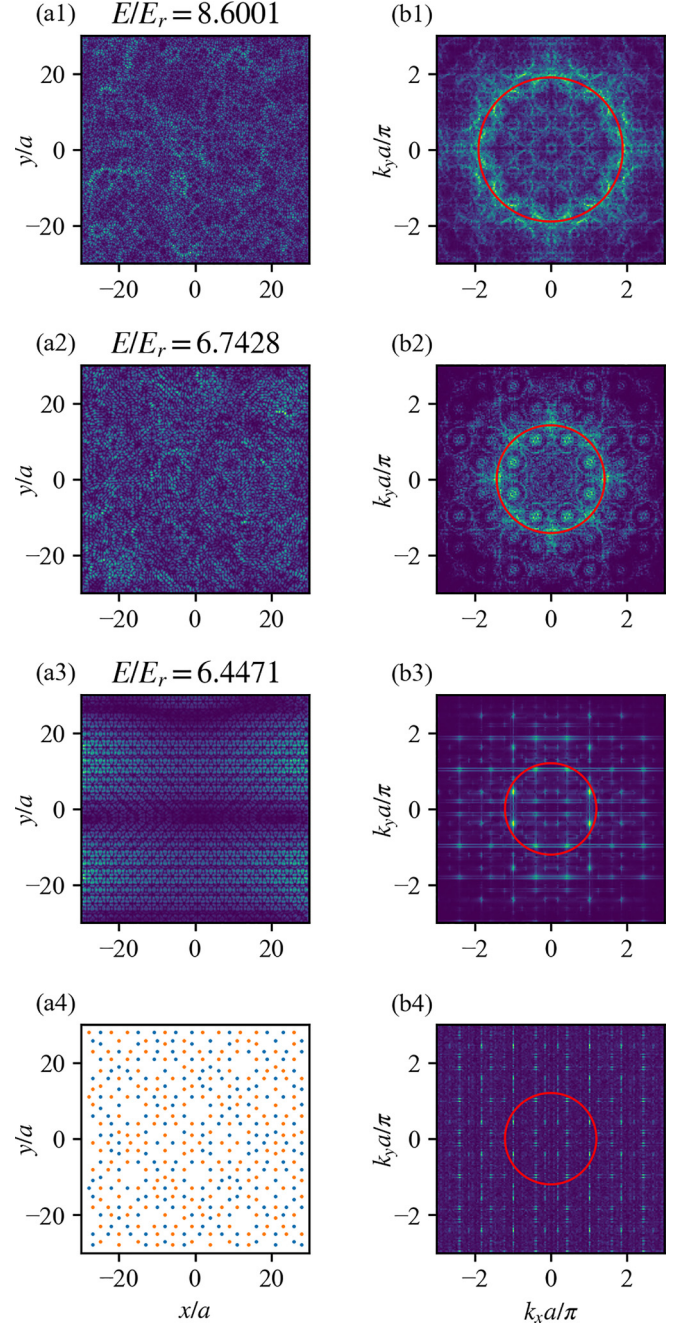


FIG. 7. Wave functions of extended states, with energies given on top of each panel, $V_0 = 2.5E_r$, and $L = 60a$. We show the (a1)–(a3) real-space density profiles and corresponding (b1)–(b3) Fourier space momentum distributions. The red circle indicates the momentum k_E given by a perturbation theory. (a4), (b4) Show the reconstructed components of (a3)–(b3) [Eq. (5)]. The spots in (a4) show the positions of the local maxima \mathbf{r}_j , with color indicating the phase (blue : $\phi_j = 0$, orange : $\phi_j = \pi$). (b4) Shows the square modulus of the Fourier transform of Eq. (5). The positions of spots in (b4) match well with those in (b3).

The formation of the momentum profile of extended states at a smaller energy is more subtle. In this case, the extended wave functions are dominated by the quasicrystal potential and we now have a quasiperiodic, latticelike structure [Fig. 7(b3)]. The origin of this structure can be deduced

as follows. First, we note that the extended state in real space is made of hybridized ring states with three node lines. The rings are located around some potential maxima, which form a discrete lattice in real space, shown in Fig. 7(a4). The wave function can thus be approximated as

$$\psi(\mathbf{r}) \simeq \int d\mathbf{r}' \psi_0(\mathbf{r}) f(\mathbf{r} - \mathbf{r}') \quad (4)$$

and

$$f(\mathbf{r}) = \sum_j e^{i\phi_j} \delta(\mathbf{r} - \mathbf{r}_j), \quad (5)$$

where $\psi_0(\mathbf{r})$ is a sample of the ring states with three node lines, \mathbf{r}_j is the position of the j th potential maxima, and ϕ_j is a phase factor of either 0 or π , which gives the correct alignment of the local structures in the original wave function. The phase factor is encoded in the color (blue or orange) of the lattice points in Fig. 7(a4). To check this interpretation, we compute the Fourier transform of $f(\mathbf{r})$ in Eq. (5) and plot it in Fig. 7(b4). The result reproduces well the primary features of the momentum profile found in Fig. 7(b3), namely, the quasiperiodic, latticelike structure, and some of the most significant spots. This shows that the structure of the lowest-energy extended states is strongly related to the quasiperiodic nature of the potential. When the energy E is further increased, the quasiperiodic structure becomes less significant, with the progressive emergence of the plane-wave momentum circles observed in Figs. 7(a1) and 7(a2).

D. Critical states

Critical states generally appear in-between the localized states not far from the edges of energy bands (see Fig. 5). The critical states typically extend across the full system, with complex geometrical patterns, separated in two main classes, illustrated in Figs. 8 and 9.

On the one hand, Fig. 8 displays the states with energy closest to $E = 4.6218E_r$ for different system sizes. For this energy, the scaling exponent is $\gamma = -1.49 \pm 0.24$, clearly different from 0 and -2 . As visible on Fig. 8(a), these critical states are all composed of small rings, similar to localized states with no node lines in the rings as in Fig. 6(e). These critical states, which contain a countless number of the small rings, have energies slightly smaller than the localized states containing only one or a few small rings, owing to hybridization, which minimizes the tunneling energy. Since the ring states that form the building blocks of such critical states are roughly isotropic, they do not favor any clear direction, and, on a larger scale, they group together and form larger ring structures containing eight small rings, and eventually form a “ring of ring” [see Fig. 8(b)]. On even larger scales, these rings of rings also group together forming more complex structures [see Figs. 8(c)–8(h)].

On the other hand, Fig. 9 shows an example of the other class of critical states, found at a higher energy. It displays the states with energy closest to $E = 5.803E_r$ for different system sizes. Here the scaling exponent is $\gamma = -0.87 \pm 0.18$, also corresponding to critical states. However, unlike Fig. 8,

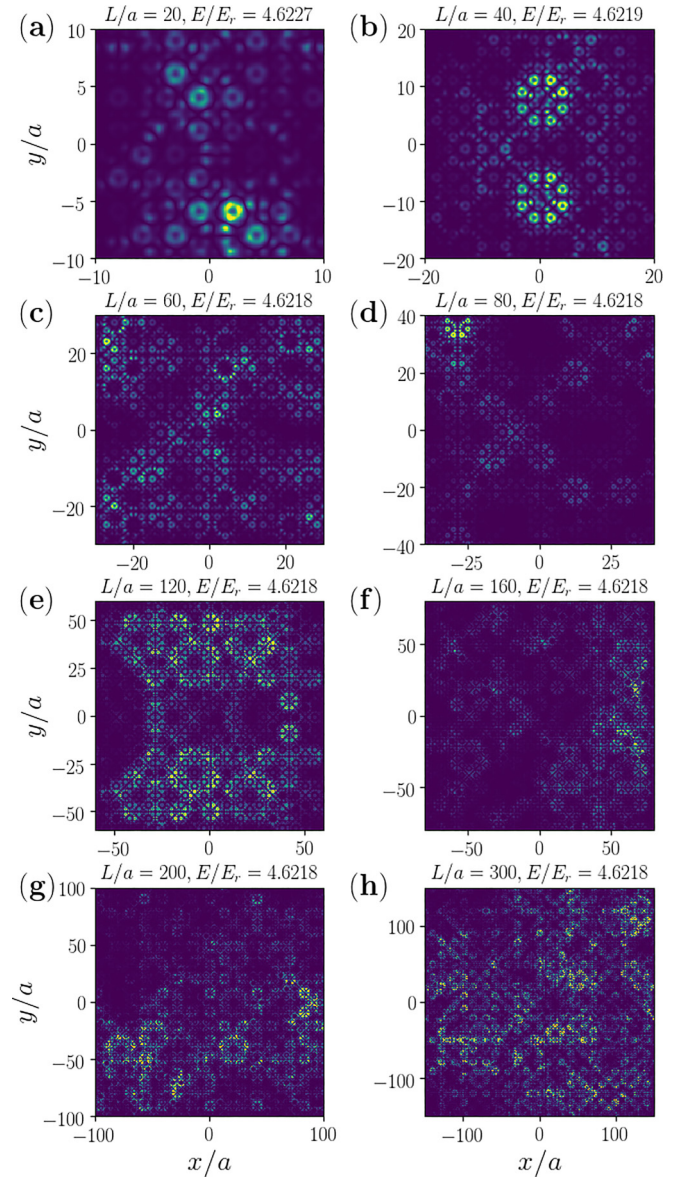


FIG. 8. Wave functions in the critical regime at $E \simeq 4.6218E_r$ for $V_0 = 2.5E_r$, shown at different scales. The various panels show the wave function of the state with eigenenergy closest to $E = 4.6218E_r$ for system sizes increasing in the reader order, from (a) $L = 20a$ to (h) $L = 300a$. Note that the colors have been rescaled to increase the contrast.

which contains rings at different scales, Fig. 9 displays square-shaped structures. On large enough scales, we find that these states display straight lines either along the main axes (x and y) or along the diagonals. In fact, these states are also built from ring states, but here with two node lines, similar to that shown on Fig. 6(g). For such ring states with node lines along the diagonals, hybridization is favored along the main axes, which maximizes the overlap of wave functions from adjacent rings. This explains the appearance of lines along the main axes. Moreover, owing to the eightfold rotation symmetry of the potential, there are also ring states with two node lines, but now oriented along the main axes. For such states, the hybridization is then favored along the diagonals, which creates the distinct lines across the diagonals.

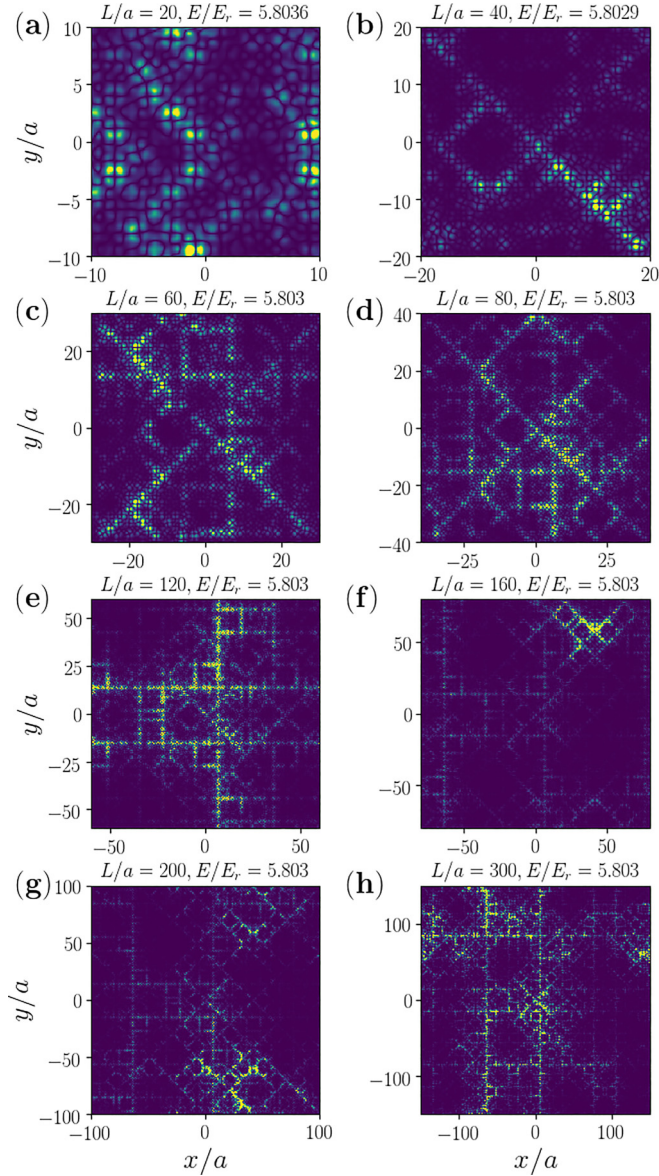


FIG. 9. Wave functions in the critical regime at $E \simeq 5.803E_r$ for $V_0 = 2.5E_r$, shown at different scales. The various panels show the wave function of the state with eigenenergy closest to $E = 5.803E_r$ for system sizes increasing in the reader order, from (a) $L = 20a$ to (h) $L = 300a$. Note that the colors have been rescaled to increase the contrast.

Finally, since all the ring states with two node lines along either the main axes or along the diagonals are quasidegenerate, squarelike structures oriented in either direction also hybridize, hence forming the complex structure observed in Fig. 9. In support of this interpretation, zooms of the wave function show that the lines parallel to the main axes are formed of ring states with two node lines along the diagonals while the lines along the diagonals are formed of ring states with two node lines along the main axes (see Appendix C).

For completeness, we have also inspected the critical states near $E \simeq 4.8E_r$, which now have one node line across their local center. Some examples are shown in Appendix C.

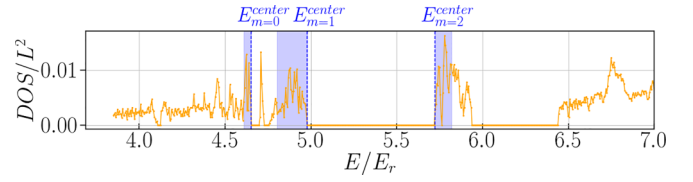


FIG. 10. Density of states per unit area versus energy for potential amplitude $V_0 = 2.5E_r$ and system size $L = 80a$. The energies of the centered small rings with winding $m = 0, 1$, and 2 are indicated by the dashed lines. The shaded areas indicate the regions of the corresponding off-centered rings with the same winding numbers.

V. GAPS BOUNDED BY RING STATES WITH PHASE WINDING

We now study the structure of the energy spectrum. The DOS for the quasicrystal with amplitude $V_0 = 2.5E_r$ and a large system size $L = 80a$ is shown in Fig. 10. It displays two main gaps, in the energy windows $E/E_r \in [4.98, 5.72]$ and $E/E_r \in [5.94, 6.44]$, respectively, as well as three smaller gaps at $E/E_r \simeq 4.11$, $E/E_r \simeq 4.65$, and $E/E_r \simeq 4.71$. To understand the origin of these energy gaps, we study the properties of eigenstates in the vicinity of the band edges.

A. Ring states at band edges

States localized in small ring structures of the potential play an important role in the energy spectrum, as also observed in Ref. [75]. For instance, the states right before the small gap at $E \simeq 4.65E_r$ are composed of small rings with a roughly homogeneous density, similar to that shown in Fig. 6(e), and spread over different locations. The states right before the first large energy gap at $E/E_r \in [4.98, 5.72]$ are similar ring states but with one node line, similar to that shown in Fig. 6(f). The states right after the same large gap are also ring states but with two node lines, similar to that shown in Fig. 6(g). The energies of ring states with 0, 1, or 2 node lines are highlighted with the shaded blue areas in Fig. 10.

Although we have so far excluded the symmetry center of the potential by considering off-centered systems, it is useful to reincorporate it in the discussion of these ring states. Indeed, very regular ring states exist for the eightfold quasicrystal potential around the symmetry center at $\mathbf{r} = 0$ [see Fig. 11(a)]. Remarkably, these centered ring states have energies that exactly limit certain bands, as indicated by the vertical, dashed blue lines in Fig. 10. For instance, the centered ring state with no node lines [Fig. 11(a1)] is the very last state of the energy band before the small gap at $E \simeq 4.65E_r$. Then, there are two degenerate centered ring states with a single node line each [Figs. 11(a2) and 11(a3)], which lie immediately before the first large gap, at $E \simeq 4.98E_r$. Finally, there are another two degenerate, centered ring states with two node lines [Figs. 11(a4) and 11(a5)] immediately after the first large gap, at $E \simeq 5.72E_r$. The other ring states with 0, 1, or 2 node lines that are situated in rings away from the center of the quasicrystal are slightly distorted [see Figs. 11(b1)–11(b5)], and their energies lie deeper in the energy bands, as indicated by the shaded areas in Fig. 10. As discussed below, rejection of the off-centered ring states inside the energy bands may be interpreted as a level repulsion effect.

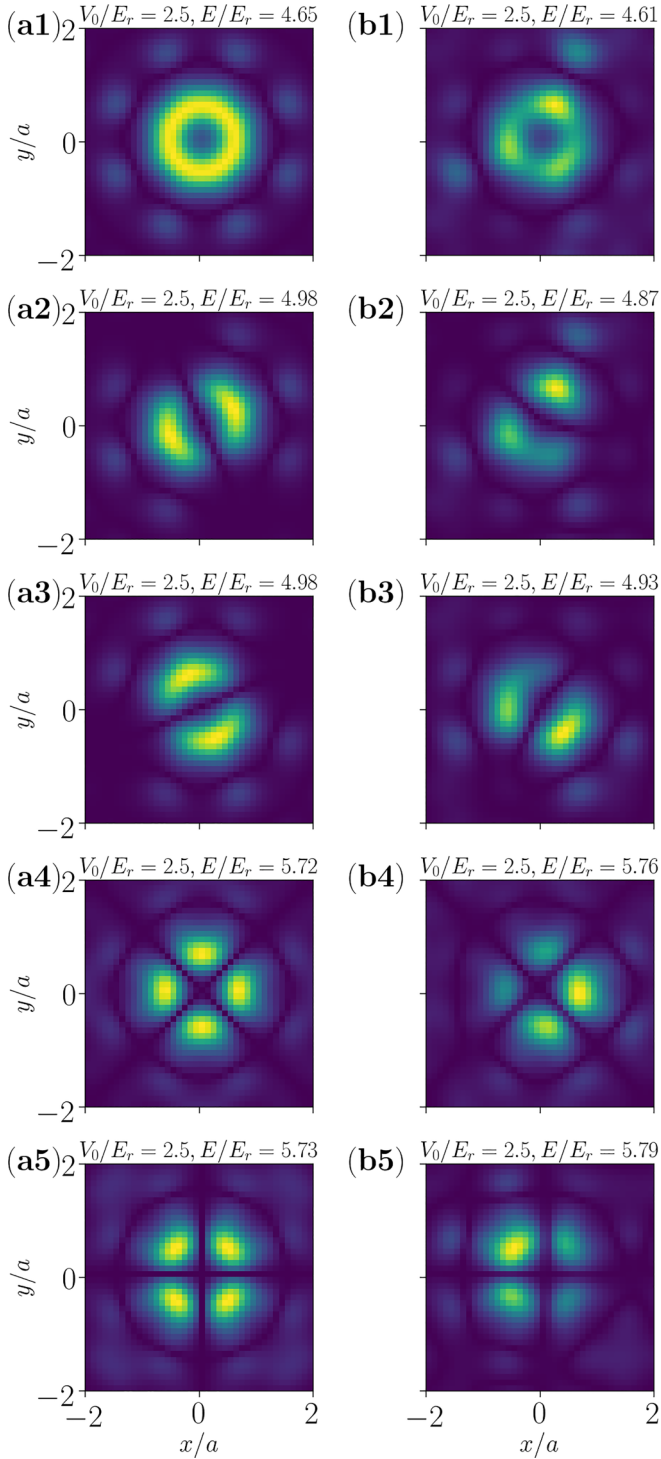


FIG. 11. Centered (left) and off-centered (right) ring states in the eightfold quasicrystal potential centered at $\mathbf{r}_0 = (0, 0)$, with amplitude $V_0 = 2.5E_r$. (a1)–(a5) States at energy band edges: (a1) last state before the small gap at $E/E_r \simeq 4.65$; (a2), (a3) two almost degenerate states immediately before the first large gap in $E/E_r \sim [4.98, 5.72]$; (a4), (a5) two almost degenerate states immediately after the same first large gap. They are eigenstates for the smallest ring around $\mathbf{r} = 0$ with winding numbers (node line numbers) $m = 0, \pm 1, \pm 2$. (b1)–(b5) Off-centered ring states around $\mathbf{r}_0 = (19.06a, 4.95a)$ obtained by diagonalization in a square with size $L = 4a$.

For the sake of completeness, note that the first state after the second large gap at $E \simeq 6.44E_r$ is made of ring states with three node lines. In this case, however, many such rings are connected, hence forming a quite compact extended state. The states at the band edges of the gap at $E/E_r \simeq 4.11$ are localized states, and will be briefly discussed later in Sec. V E. Finally, the states at the other band edges before $E \simeq 6.44E_r$ are also localized states, without any particular features in their patterns.

These observations indicate that the small ring states, especially the ones centered on the symmetry center of the quasicrystal potential at $\mathbf{r} = 0$, play special roles in the structure of the spectrum, and we discuss them in more detail below.

B. Central ring

We first consider the ring states around the quasicrystal symmetry center at $\mathbf{r} = 0$ [see Fig. 11(a)]. They are located in a nearly isotropic annular potential well of radius $\rho_0 \simeq 0.61a$. More precisely, the potential has eight very shallow potential wells along the ring, which may, however, be neglected. In particular, we find that the ring state with no node, Fig. 11(a1), has a nearly isotropic density with modulations less than 10%. As a result, the small ring states in Fig. 11(a) may be approximated by states localized in the nearly isotropic annular potential well with almost isotropic density and $O(2)$ rotational symmetry around the symmetry center $\mathbf{r} = 0$. In the vicinity of the annular well, the Hamiltonian and the planar angular momentum operator \hat{L}_z can be diagonalized simultaneously, and the wave functions can be written as $\phi_m^0(\mathbf{r}) \simeq u_m(r)e^{im\theta}$, where $u_m(r)$ is a real-valued function, θ is the polar angle, and $m \in \mathbb{Z}$ is the phase winding number. For sufficiently strong potential amplitude V_0 and low winding number m , the functions $u_m(r)$ are strongly confined around $r = \rho_0$ and we may neglect the m dependence originating from the centrifugal term. For details, see Appendix D 1. Figure 11(a1) is the state with winding number $m = 0$. The states in Figs. 11(a2) and 11(a3) correspond to winding numbers $m = \pm 1$. Since the states $\phi_{\pm 1}^0(\mathbf{r})$ are strictly degenerate, any linear combination of both is also an eigenstate of the Hamiltonian. Numerical diagonalization returns real-valued wave functions, i.e., $\psi_{+1}^0(\mathbf{r}) \simeq \sqrt{2}u(r)\cos(\theta - \theta_1)$ and $\psi_{-1}^0(\mathbf{r}) \simeq \sqrt{2}u(r)\sin(\theta - \theta_1)$, where θ_1 is some reference angle. Consequently, the two states in Figs. 11(a2) and 11(a3) show orthogonal node lines at the angles $\theta_1 + \pi/2$ and θ_1 , respectively. The angle θ_1 is determined by the small modulations of potential along the annular well and, in the numerics, by the discretization, which does not satisfy an exact eightfold rotation symmetry. Similarly, Figs. 11(a4) and 11(a5) show states with two node lines, corresponding to linear combinations of the two degenerate states with winding numbers $m = \pm 2$, $\psi_{+2}^0(\mathbf{r}) \simeq \sqrt{2}u(r)\cos(2\theta - \theta_2)$, and $\psi_{-2}^0(\mathbf{r}) \simeq \sqrt{2}u(r)\sin(2\theta - \theta_2)$, with some angle θ_2 .

We now check the validity and accuracy of our model. On the one hand, because of their strong localization, we can find the exact centered ring states by performing diagonalization in a small square around $\mathbf{r} = 0$ with size $L = 4a$, larger than the ring diameter $2\rho_0 \simeq 1.2a$. Figure 12(a) shows the

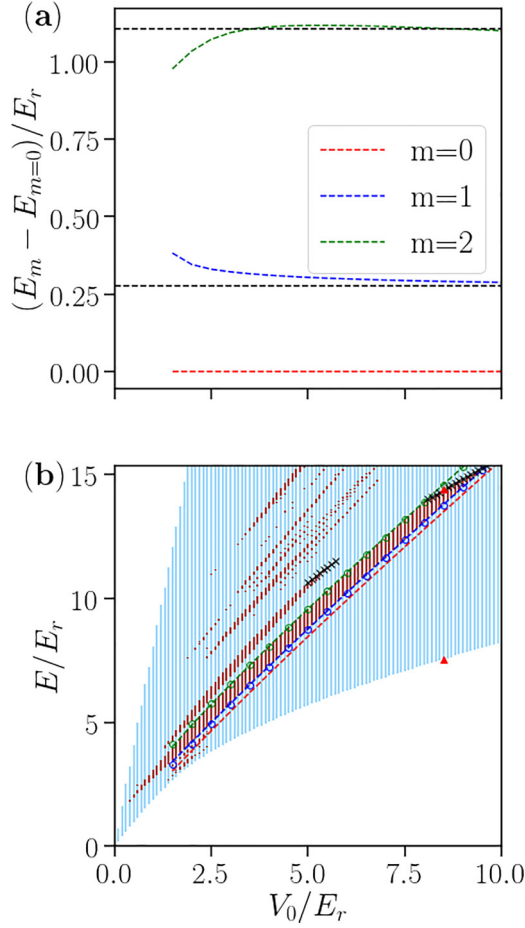


FIG. 12. Centered ring states. (a) Energy differences $E_m - E_0$ between the ring states with winding numbers $m = \pm 1$ (blue) and ± 2 (green), and the ring state with winding number $m = 0$ (red, zero by construction). The dashed black lines show the corresponding theoretical estimates $\hbar^2 m^2 / 2M\rho_0^2$ [see Eq. (6)] for $m = \pm 1$ and ± 2 . (b) Energy spectrum (reproduced from Fig. 3) showing bands (blue) and gaps (red). The dashed lines show the energies of the ring states E_m obtained from diagonalization in a small system with size $L = 4a$ for $m = \pm 1$ (blue) and $m = \pm 2$ (green). The circles are the theoretical estimates using Eq. (6) with E_0 corresponding to the numerical value. The black crosses show the energies of states which enter and finally close the large gaps at large V_0 , and the two red triangles correspond to the two states plotted in Fig. 14 (see discussion in Sec. VD).

eigenenergies hence obtained subtracted by the eigenenergy of the state with winding number $m = 0$ (dashed red line, zero by construction), i.e., $E_m - E_0$ for $m = \pm 1$ (dashed blue line) and $m = \pm 2$ (dashed green line). On the other hand, according to our model, the energies of the centered ring states only differ by their orbital rotation energy, which can be written as

$$E_m \simeq E_0 + \frac{\hbar^2 m^2}{2M\rho_0^2}, \quad (6)$$

where we have neglected the m dependence of the radial Hamiltonian as well as the radial extension of $u(r)$ around the radius of the ring ρ_0 . The results of this prediction are shown as dashed black lines in Fig. 12(a), which correspond

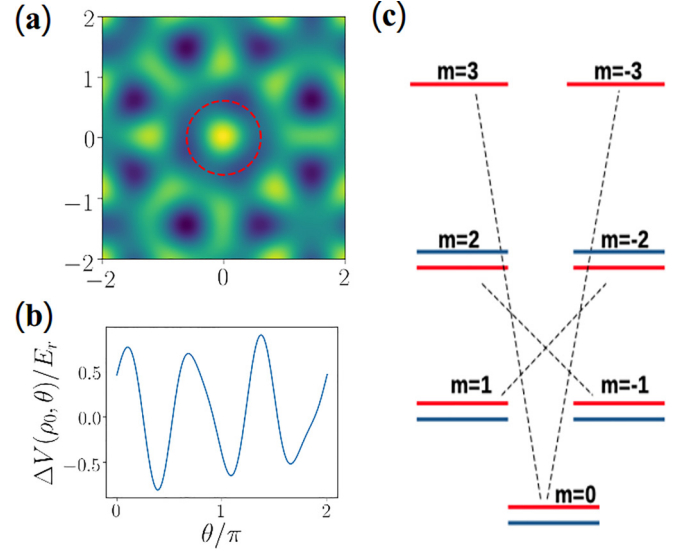


FIG. 13. Off-centered ring states. (a) Quasicrystal potential in the vicinity of an off-centered annular potential well, centered at $\mathbf{r}_0 = (19.06a, 4.95a)$. Color scales represent the potential from low values (dark purple) to high values (light yellow). The dashed circle is the ring of radius $\rho_0 = 0.61a$ around the local maximum. (b) Perturbation potential $V(\rho_0, \theta)$ along the ring as a function of the polar angle θ . (c) Sketch of the energy-level repulsion picture. The red lines represent energy levels of the centered (unperturbed) ring states with different winding numbers, and the blue lines their off-centered (perturbed) counterparts. The dashed lines represent the dominant couplings.

to the orbital rotation energy for winding numbers $m = \pm 1$ and ± 2 , respectively. As expected, we find an increasingly better estimate of the ring state energies as the amplitude of the quasicrystal potential increases, owing to a stronger radial confinement. In addition, the energies of these ring states are also plotted on top of the full spectrum for a large system of size $L = 60a$ in Fig. 12(b). The full spectrum is reproduced from Fig. 3, with blue denoting the bands and red the gaps. The dashed lines show the energies of the ring states E_m with $m = 0$ (red), $m = \pm 1$ (blue), and $m = \pm 2$ (green) as obtained from diagonalization in a small system with size $L = 4a$ and the open disks represent the corresponding theoretical estimates [Eq. (6)]. The ring state energies lie on the bands' edges. This is consistent with the fact that the large gap is created by the centered, localized ring states with winding number $m = \pm 1$ and ± 2 , before it starts to close at $V \simeq 8E_r$.

C. Off-centered rings

Let us now examine the off-centered ring states, which are located in annular potential wells around various positions away from the symmetry center of the quasicrystal potential. A typical example is shown in Fig. 11(b), which corresponds to ring states centered at $\mathbf{r}_0 = (19.06a, 4.95a)$ with 0, 1, or 2 node lines. Quasiperiodicity of the system implies that the potential around such states is similar to that around the central ring, but with distortions. The latter are weak but clearly non-negligible [see Fig. 13(a)]. In particular, the potential and the ring states do not strictly fulfill eightfold rotation symmetry

around the local center at $\mathbf{r}_0 \neq 0$ [see in particular the appearance of three deeper wells around the central ring (dashed red line)]. As a consequence, the corresponding ring states, Figs. 11(b1)–11(b5), are not as symmetric as the centered ones, Figs. 11(a1)–11(a5). Nevertheless, the off-centered ring states have nearly the same radius as the centered one, $\rho_0 \simeq 0.61a$, and can still be classified according to their winding number or, equivalently, node line number m . Similar properties are found around other ring states centered at different locations.

As mentioned above, we have observed that the off-centered ring states with winding number $m = 0$ or ± 1 have lower energy than their centered counterparts. In contrast, for winding number $m = \pm 2$, the off-centered ring states have a higher energy than their centered counterparts. This phenomenon is due to level repulsion, as we show now. Owing to the similarity of the off-centered annular potential wells and ring states with their centered counterparts, we may understand the properties of the former as a perturbation of the latter. To lowest perturbation order, we write the off-centered ring states as the shifted centered one $\phi_m(\mathbf{r}) \simeq \phi_m^0(\mathbf{r} - \mathbf{r}_0)$ and the perturbation potential as $\Delta V(\mathbf{r}) = V(\mathbf{r}) - V(\mathbf{r} - \mathbf{r}_0)$. Working in the sub-Hilbert space of these states, the perturbation matrix elements are

$$\langle \phi_{m_1} | \Delta V | \phi_{m_2} \rangle \propto \int d\theta \Delta V(\rho_0, \theta) e^{i(m_2 - m_1)\theta}. \quad (7)$$

On the one hand, the left-hand side of Eq. (7) can be calculated numerically, where the required wave functions are reconstructed by linear combination of the real-valued numerical wave functions, using $\phi_m(\mathbf{r}) = [\psi_{+m}(\mathbf{r}) + i\psi_{-m}(\mathbf{r})]/\sqrt{2}$ for $m \in \mathbb{Z}$. On the other hand, the right-hand side is found by neglecting the radial extension of the ring states and $\Delta V(\rho_0, \theta)$ is a shorthand notation for the perturbed potential along the ring of radius ρ_0 with θ the polar angle. Due to the three-period oscillation of the potential around the ring shown in Fig. 13(b), the Fourier integral in Eq. (7) shows two resonances for $m_2 - m_1 = \pm 3$, and we expect that the couplings are dominated by the processes such as $m \leftrightarrow m \pm 3$. We indeed find that the corresponding couplings are at least one order of magnitude larger than the other ones (see perturbation matrix for winding numbers up to $|m| = 3$ in Appendix D 2). Since perturbation is stronger for states with closer unperturbed eigenenergies, the strong couplings between $m \leftrightarrow m \pm 3$ effectively create a two-level system for states $|m = +1\rangle$ and $|m = -2\rangle$ on the one hand, and for states $|m = -1\rangle$ and $|m = +2\rangle$, on the other hand. The state $|m = 0\rangle$ is strongly coupled to both states $|m = 3\rangle$ and $|m = -3\rangle$, hence forming a three-level system. The overall effective system is sketched in Fig. 13(c). Energy-level repulsion in the two-level systems shifts down the energies of the states with winding number $m = \pm 1$ and up the energies of the states with winding number $m = \pm 2$. Note that the diagonal perturbation terms $\langle \phi_m | \Delta V | \phi_m \rangle$ are negligible. The couplings between state $|m = 0\rangle$ and states $|m = 3\rangle$ and $|m = -3\rangle$ shift down the energy of $|m = 0\rangle$ since off-diagonal perturbations always yield negative corrections to the ground-state energy.

As a result, the energies for the off-centered ring states with windings $m = 0, \pm 1, \pm 2$ are shifted in specific directions,

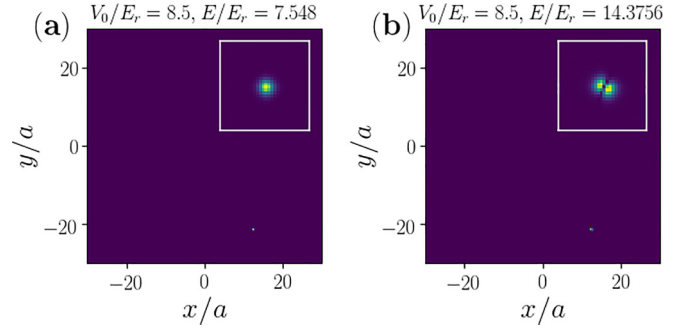


FIG. 14. (a) Ground state of the system alongside (b) the first state after the first large energy gap, corresponding to the two red triangles in Fig. 12(b). The system size is $L = 60a$ and the potential amplitude is $V_0 = 8.5E_r$. The insets show magnifications of the strongly localized states.

which is in agreement with our numerical diagonalization. As the largest energy gap corresponds to that between ring states with winding numbers $m = \pm 1$ on the one hand and $m = \pm 2$ on the other hand, we have shown that the bottom of this gap is bounded by the winding $m \pm 1$ ring states at center $\mathbf{r} = 0$. Likewise, the top of this gap is bounded by the winding $m = \pm 2$ ring states at center $\mathbf{r} = 0$. This persists in the thermodynamic limit, and the gap width is just the energy difference between these centered ring states.

D. Closing of gaps

Our model relates the large gaps to ring states with different winding numbers. According to Eq. (6), valid for strong radial confinement, the gap widths may thus be expected to reach a constant value for large enough potential depth V_0 [see also Fig. 12(a)]. Consistently, we indeed observe that the blue and green dashed lines in Fig. 12(b), which show the energies of the centered ring states with winding numbers $m = \pm 1$ and ± 2 , respectively, are almost parallel to each other. They match the boundaries of the largest gap, shown in red, for a significant energy range, for $2 \lesssim V_0/E_r \lesssim 8.1$. However, this gap, as well as the next one right above, close progressively, respectively, in the ranges $8.1E_r \lesssim V_0 \lesssim 9.6E_r$ and $5E_r \lesssim V_0 \lesssim 5.7E_r$; see the black crosses in Fig. 12(b), which indicate the upper limit of the gaps in these regions. In fact, the closing of both these gaps is due to another kind of strongly localized states. For weak potential amplitude V_0 , the latter have an energy well inside an energy band above the second gap, but when V_0 increases, they enter successively each gap between the ring states and create the new upper limit of the gaps. The state closing the largest gap for $V_0 = 8.5E_r$ [upper red triangle in Fig. 12(b)] is shown in Fig. 14(b) and, for comparison, the ground state of the system [lower red triangle in Fig. 12(b)] is shown in Fig. 14(a).

Both these states turn out to be strongly localized in the same deep potential well, and correspond to the ground state and the first excited state of this well. More precisely, we may approximate the deep potential well by a harmonic potential. The state in Fig. 14(a) is then the ground state of the trap, while the state in Fig. 14(b) is the first excited state of the same trap. Consistently with this interpretation, we note that the

local minimum of the trap has a vanishingly small potential energy and the energy of the excited state in Fig. 14(b) is about twice that of the state in Fig. 14(a) (see values on top of the figures). This is what is expected for a 2D isotropic harmonic trap. The discrepancy to exact energy doubling (about 5%) may be attributed to slight anisotropy and/or anharmonicity of the trap. Such kind of deep potential wells spread over the system and similar states as in Fig. 14 located around these potential wells are found with similar energies. As the potential amplitude increases, the first excited states of such deep potential wells, similar to Fig. 14(b), enter the higher large gap at about $V_0 \simeq 5E_r$ and completely close it at about $V_0 \simeq 5.7E_r$. Then, as the potential amplitude further increases, those states enter the lower large gap at about $V_0 \simeq 8.1E_r$ and close it at about $V_0 \simeq 9.6E_r$ [see black crosses in Fig. 12(b)]. A similar phenomenon explains why we do not observe gaps at a higher energy. In principle, Eq. (6) suggests even larger gaps at higher energies. However, we find that various kinds of states other than the ring states appear inside the gaps induced by the sole ring states and the latter are not visible. Moreover, these different kinds of states hybridize at high energy and the structure of the spectrum is not governed by clear ring states any more.

E. Self-similarity and minigaps

The spectrum in Fig. 3 presents self-similar structures. Figure 15(a) shows a zoom of the latter around $V_0 = 2E_r$ and $E = 3.5E_r$. It clearly shows several gaps, the lowest two, for instance, around energy $E \simeq 3.4E_r$ for $V_0 = 1.9E_r$, and different energy for different V_0 . Although these gaps are almost invisible on Figs. 3 and 12(b), we have checked that they are legitimate gaps, according to the procedure presented in Appendix A. To identify the nature of these gaps, the states at their edges are plotted in Figs. 15(b)–15(e). Figure 15(b) shows the state at the bottom edge of the first gap. It is a state localized around the quasicrystal center $\mathbf{r} = 0$ and it is composed of eight spots corresponding to eight local potential wells. The latter are identical to each other due to exact eightfold rotational symmetry around $\mathbf{r} = 0$. They lie on a ring larger than the small ring discussed above [shown for reference as a dashed red circle in Figs. 15(b), 15(c), and 15(e)]. The states localized on this larger ring can still be classified according to their winding numbers or equivalently node line numbers. The state in Fig. 15(b) shows one clear node line and it has thus winding number $m = \pm 1$. Similarly, Fig. 15(c) shows the state with winding number $m = \pm 2$, which lies near the top of the first gap, and the state at the top of the second gap shown in Fig. 15(e) that with winding number $m = \pm 3$. Note that the state of Fig. 15(c) is not strictly at the top of the first gap. The state at the very top edge of the first gap is composed of four off-centered copies of Fig. 15(c) connected together and has a slightly lower energy than the centered state shown in Fig. 15(c). The state at the bottom edge of the second gap shown in Fig. 15(d) is not localized at $\mathbf{r} = 0$ and has no clear special structure.

The general picture of these small gaps is thus similar to that of the large gaps discussed above created by the small ring states with different winding numbers. The only difference is

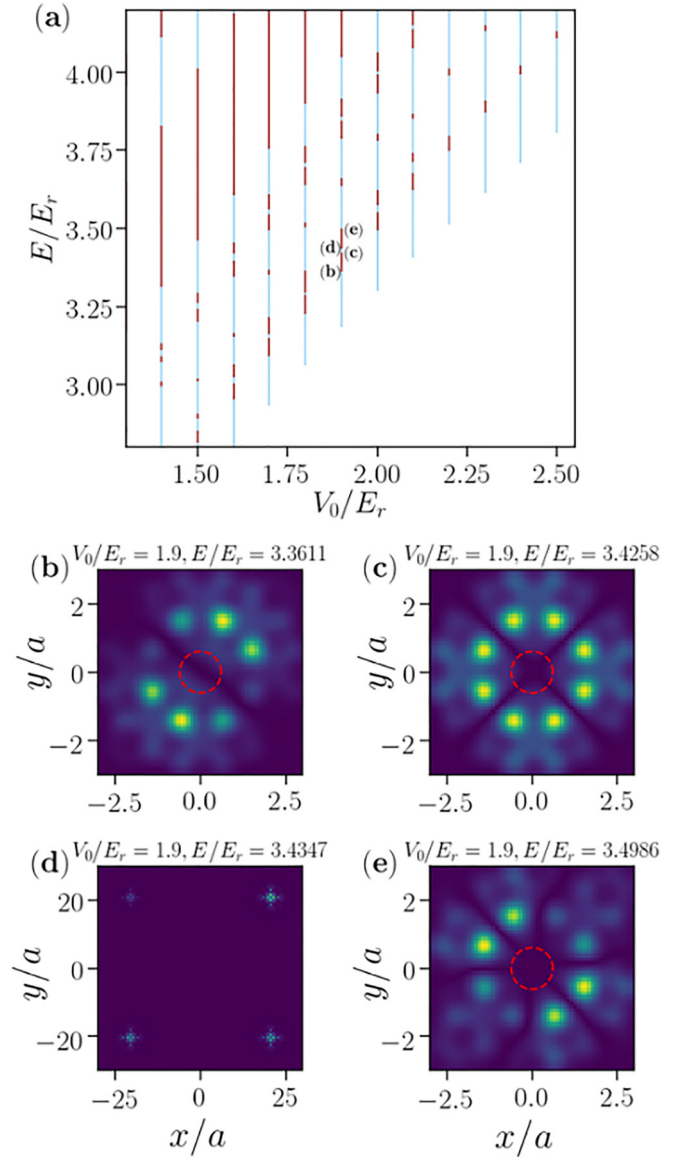


FIG. 15. (a) Zoomed spectrum of the eightfold quasicrystal potential for various amplitudes V_0 . Bands are colored blue and red. (b)–(e) Eigenstates at band edges of the two gaps with energy around $E = 3.4E_r$ for $V_0 = 1.9E_r$. (b), (c) Bottom and top states of the first gap. (d), (e) Bottom and top states of the second gap.

that the ring states creating the small gaps have a larger ring radius, so that the energy differences due to phase windings are much smaller, and the gap sizes are comparatively much smaller than the gaps created by the small rings.

VI. QUASICRYSTAL POTENTIALS WITH DIFFERENT ROTATIONAL SYMMETRIES

So far, we have considered the localization and spectral properties of a quasicrystal potential with eightfold rotational symmetry. Here we briefly discuss whether or not quasicrystals with different rotational symmetries may also possess similar properties. To answer this, we study quasicrystal potentials that are generated by interfering a larger number n of laser beams. The general formula

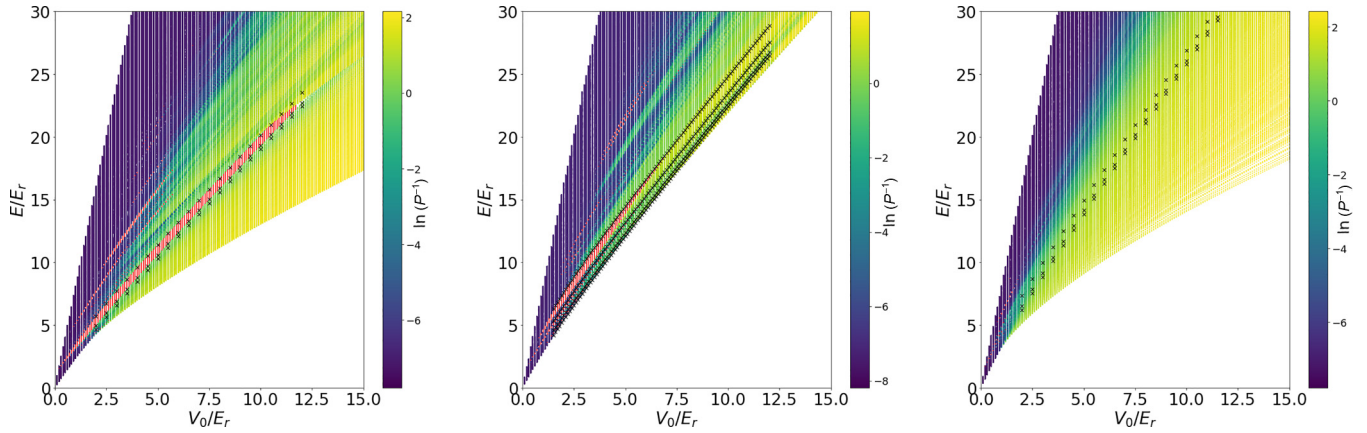


FIG. 16. Energy spectra of quasicrystal potentials with different rotational symmetries as created by n pairs of counterpropagating laser beams, with $n = 5$ (left, 10-fold), $n = 6$ (middle, 12-fold), and $n = 7$ (right, 14-fold). The system size is $L = 60a$, centered at $x = -13543a$, $y = 196419a$. The color scale represents the value of $\ln(P^{-1})$ of each eigenstate, while the gaps are all colored red. The energies of the first few centered ring states are shown as black crosses.

of a quasicrystal potential with a $2n$ -fold rotational symmetry is

$$V(\mathbf{r}) = V_0 \sum_{k=1}^n \cos^2(\mathbf{G}_k \cdot \mathbf{r} + \phi_k), \quad (8)$$

with $\mathbf{G}_k = \frac{\pi}{a}[\cos(k\pi/n), \sin(k\pi/n)]$. Realization of such potentials has been recently proposed in Ref. [82]. In Fig. 16, we plot the energy spectra for $n = 5, 6$, and 7 . The general localization picture is similar to that previously discussed for the eightfold quasicrystal potential ($n = 4$): For sufficiently large amplitude V_0 , the eigenstates are typically localized at low energy and extended at high energy. At intermediate energy, we find a nonmonotonous energy dependence of the localization strength. Moreover, for $n = 5$ or 6 , the spectrum also has at least one large gap, similar to that found for $n = 4$, as well as smaller but visible gaps. For $n = 7$ instead, the gaps become much narrower and almost invisible at the scale of Fig. 16. To understand the origin of these gaps, we note that the quasicrystal potentials created by more than four laser pairs also have an annular potential well around the center at $\mathbf{r} = 0$, with almost the same radius $\rho_0 \simeq 0.61a$. As a result, this annular potential well also hosts ring states with different winding numbers, the energies of which are still approximately given by Eq. (6). The energy differences are thus almost the same as for $n = 4$, but the reference energy E_0 may be dependent on n . Moreover, they are almost independent of the potential amplitude for large enough V_0 . The energies of the first few centered ring states for each quasicrystal potential are plotted as black crosses in Fig. 16.

For $n = 5$, the structure of the spectrum is very similar to that discussed above for $n = 4$. In particular, the largest gap is also created by the gap between the ring states with winding numbers $m = \pm 1$ and ± 2 , and the gap width is almost the same as for $n = 4$. For $n = 6$, the largest gap may also be related to ring states, now with winding numbers $m = \pm 2$ and ± 3 , and the gap size is larger. More precisely, the top of the gap is indeed composed of centered ring states with winding number $m = \pm 3$. In contrast, the bottom of the gap is not strictly a centered ring state with winding number

$m = \pm 2$ since off-centered ring states with the same winding number have higher energies than the centered one, as discussed above. For a limited range of quasicrystal amplitude, $2E_r \lesssim V_0 \lesssim 4E_r$, the centered and off-centered ring states with $m = \pm 2$ lie near by the band edge, but the true edge state turns out to be a different state, which can be either localized or extended with a complex structure, depending on V_0 . For $V_0 \gtrsim 4E_r$, new localized states enter the bottom of the gap, and progressively close it from below. Note also that for a certain range of V_0 , roughly between $2E_r$ and $7E_r$, the ground state of the whole spectrum is the centered ring state with winding number $m = 0$. Finally, we find that for $n = 7$ the gaps have almost negligible sizes, and there is no large gap near the energies of the ring states. This is because other kinds of states coexist with those ring states in the same eigenenergy ranges, even though ring states still have the same energy differences for different winding numbers. For larger n , we found that large gaps generated by ring states remain closed.

VII. CONCLUSION AND DISCUSSION

In summary, we have shown that 2D optical quasicrystals host exotic localization properties and intriguing spectral features. For the eightfold rotationally symmetric potential, a finite-size scaling analysis of the IPR reveals the presence of localized, critical, and extended states. Extended states dominate the energy spectrum at large energies, while localized states populate the low-energy spectrum, as expected. However, at intermediate energies, we find that localized states can appear alongside critical states, with no clear separation between them. Furthermore, large gaps appear in the spectrum, with some states at the band edges having a strongly localized profile. These localized states can take the form of ring states with different quantized winding numbers. By modeling these ring states, we have found that the band edges coincide with the theoretical energy of ring states, thus confirming that they play an important role in the formation of energy gaps within optical quasicrystals. Finally, we have also confirmed that quasicrystals with other rotational symmetries can also possess similar kinds of localization properties and energy

spectra, with ring states again playing an important role. In all cases, the most prominent gaps of the spectra are stable across a range of potential depths V_0 and rotational symmetries, provided that other localized states do not compete or enter the gap generated by the ring states. Our results shed light on localization and spectral properties of optical quasicrystal potentials, as realized in recent experiments [42,69,76,82]. Further application and development of this work may be expected in two directions.

On the one hand, our results are directly applicable to the above-mentioned experiments. The eightfold quasicrystal potential studied in the main part of the paper has been implemented in the experiments reported in Refs. [42,69,76] and potentials with higher-order discrete rotation symmetry can be implemented in a similar manner by using a suitable number of laser beams (see, for instance, Refs. [41,82]). The quasicrystal potential amplitudes considered here, $V_0 \simeq 1 - 15E_r$, are also relevant for these experiments and interatomic interactions can be canceled with high accuracy using Feshbach resonance methods [45,83]. Localization may be unveiled in ultracold-atomic gases using expansion schemes, as proposed in Refs. [41,84] and realized, for instance, in Refs. [51,85–87] (see also Refs. [88–92]) for further theoretical discussions. In this scheme, an initially trapped ultracold-atom gas is released into the quasicrystal potential, generating a wave packet covering a tunable range of energy components. The components whose energy corresponds to a band of localized states stop expanding on a short length scale, while those whose energy corresponds to a band of extended states show normal diffusive expansion. Direct imaging at different times can thus be used to distinguish between them. For the 2D quasicrystal lattice considered here, bands of critical states also exist, for which we can anticipate anomalous diffusion, also observable in the expansion dynamics. In such scheme, a high-energy cutoff is set by the chemical potential of an initially interacting Bose-Einstein condensate or the Fermi energy of an ultracold gas of fermions. When controlled by the initial interaction strength and/or the number of atoms, we expect to observe a localized gas at low chemical potential, anomalous diffusion on top of a localized component at intermediate chemical potential, and an additional normal diffusion when the spectral range contains extended states. Note, however, the coexistence of localized, critical, and extended components may make their segregation difficult. To overcome this issue, fine selection of a particular energy may be realized using radio-frequency transfer from an internal atomic state insensitive to the quasicrystal potential towards a sensitive state [93]. Here, the width of the selected energy range is proportional to the inverse of the pulse duration and can be chosen from a band of either localized, critical, or extended states. Expansion then leads, respectively, to pure localization, anomalous diffusion, or normal diffusion. The nontransferred part undergoes ballistic expansion or can even be eliminated by transfer to a nonimaged internal atomic state. This makes it possible to reconstruct bands of localized, critical, and extended states, as shown in Fig. 5. The existence of the gaps discussed here can also be demonstrated by this approach.

On the other hand, our results on localization and spectral properties of the single-particle problem studied here also play

an important role in the physics of correlated quantum gases in a 2D quasicrystalline potential. This is particularly the case for a gas of correlated bosons. In one dimension and in the regime of strong interactions, a gas of bosons can be exactly mapped onto a gas of free fermions, a phenomenon known as fermionization. This makes it possible to map Mott insulators onto free spectral gaps and Bose glass onto localized states. In dimensions higher than one, such exact mapping breaks down, but fermionization persists nonetheless when the Bose gas populates only states that are spatially separated from one another. In this case, strong repulsive interactions suppress multiple occupation of each localized state, hence mimicking an effective Pauli principle in real space. Our results could thus help understand the onset of a Bose glass as well as a Mott plateau in the strongly interacting regime, found in recent work [74].

ACKNOWLEDGMENTS

We thank H. Yao for fruitful discussions. We acknowledge the CPHT computer team for valuable support. This research was supported by the Agence Nationale de la Recherche (ANR, Project No. ANR-CMAQ-002 France 2030), the program “Investissements d’Avenir” LabEx PALM (Project No. ANR-10-LABX-0039-PALM), the IParis Doctoral School, and HPC/AI resources from GENCI-TGCC (Grant No. 2022-A0110510300).

APPENDIX A: DENSITY OF STATES AND GAPS

Careful identification of the true energy gaps in the spectrum can be captured by performing a finite-size scaling analysis. Here we compute the density of states (DOS) using

$$g_\epsilon(E) = \frac{\delta W(E, \epsilon)}{\epsilon}, \quad (\text{A1})$$

where $\epsilon = 0.005E_r$ is a finite-energy resolution and $\delta W(E, \epsilon)$ is the number of states in the energy window $[E, E + \epsilon)$. A good estimate of the DOS is obtained when the energy resolution ϵ is smaller than the typical variation scale of the DOS and larger than the inverse of the typical DOS so that several states are in each energy slice, $g_\epsilon(E)\epsilon \gg 1$. For the homogeneous 2D gas, we have $g(E)^{-1}E_r = 4a^2/\pi L^2 \simeq 0.003$ for the smallest system size $L = 20a$.

Figure 17 shows the DOS per unit area versus energy for different system sizes from $L = 20a$ to $90a$. Each point with zero DOS gives an energy gap, so that all gaps larger than the energy resolution ϵ are revealed. For the smallest system size of $L = 20a$ in Fig. 17, the DOS displays many small gaps and a few large energy gaps. While the two large gaps are stable against increasing the system size, only a few small gaps survive for large system sizes. For the energy resolution $\epsilon = 0.005E_r$, the structure of the spectrum is stable when the system size is larger than $L \simeq 60a$.

APPENDIX B: LINEAR FIT QUALITY FOR FINITE-SIZE SCALING OF THE IPR

The exponent γ , such that $P^{-1} \sim L^\gamma$, is found from linear fits of $\ln(P^{-1})$ versus $\ln(L/a)$, with results shown in the first

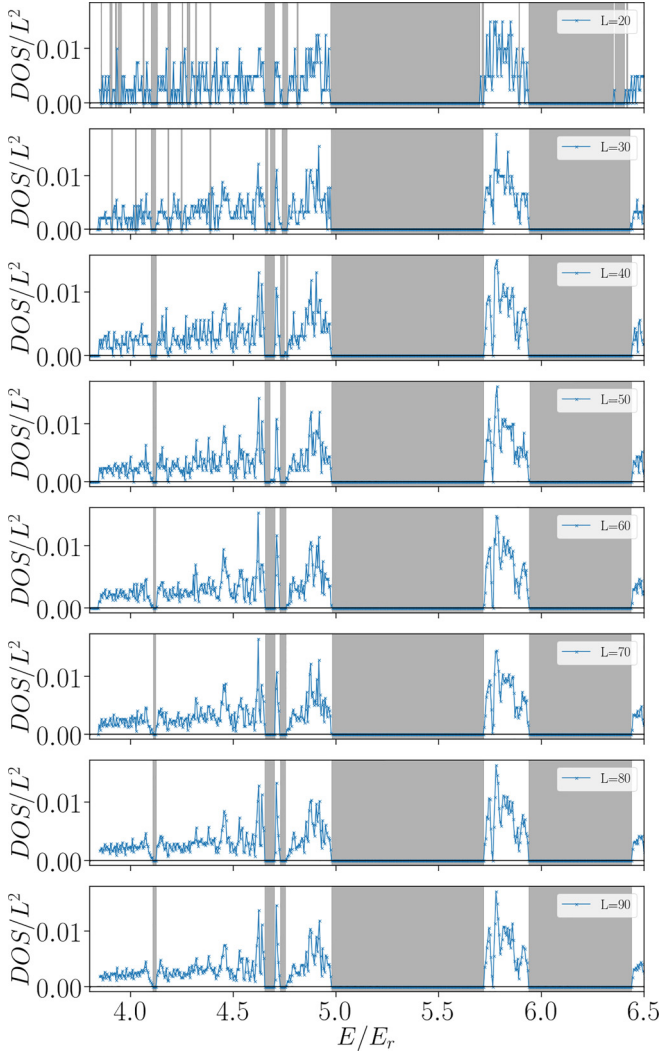


FIG. 17. Density of states per unit area versus energy for the quasicrystal amplitude $V_0 = 2.5E_r$ and the energy resolution $\epsilon = 0.005E_r$. The various panels correspond to increasing system size from $L = 20a$ (top) to $90a$ (bottom). The energy gaps are indicated by gray shaded areas.

row of Fig. 18 (same data as in the upper low of Fig. 5 in the main text). To characterize the fit quality, we compute the Pearson correlation coefficient

$$r = \frac{\sum_j (x_j - \bar{x})(y_j - \bar{y})}{\sqrt{\sum_i (x_i - \bar{x})^2 \sum_i (y_i - \bar{y})^2}} \quad (\text{B1})$$

for two data sets x_i, y_i where \bar{x} and \bar{y} are their mean values. A value of $|r|$ close to 1 indicates good linear correlation between the data sets, while $|r|$ close to 0 indicates poor linear behavior. The correlation coefficient for linear fitting of $\ln(\overline{P^{-1}})$ and $\ln(L/a)$ is shown in the second row of Fig. 18. It shows good linear behavior with $r \simeq -1$ and $\gamma \simeq -2$ for energy $E \gtrsim 6.45E_r$, and the states in this energy range are clearly extended. For a lower-energy range, however, the coefficients r are much worse, which questions the corresponding results. This is actually misleading as when the slope γ is about 0, even weak fluctuations of

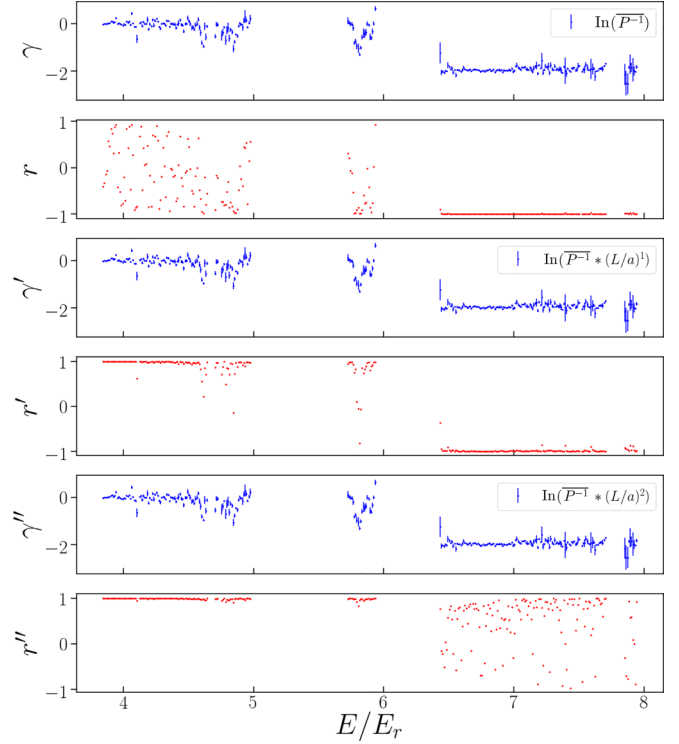


FIG. 18. Finite-size scaling of the IPR, performed as in Fig. 4, for system sizes ranging from $L = 20a$ to $100a$, except in some narrow energy windows where data for larger sizes, $L = 120a, 160a, 200a, 300a$, are also calculated. The panels, from top to bottom, show, successively the scaling exponent and the corresponding regression coefficient: (i) γ and r for $\ln(\overline{P^{-1}})$ versus $\ln(L/a)$, (ii) γ' and r' for $\ln(\overline{P^{-1}} \cdot L/a)$ versus $\ln(L/a)$, and (iii) γ'' and r'' for $\ln[\overline{P^{-1}} \cdot (L/a)^2]$ versus $\ln(L/a)$.

data points around a constant value can greatly affect the coefficients r .

To circumvent this issue, we repeat the linear regression for $\ln(\overline{P^{-1}} \cdot L/a)$ versus $\ln(L/a)$ with slope $\gamma' + 1$ and for $\ln[\overline{P^{-1}} \cdot (L/a)^2]$ versus $\ln(L/a)$ with slope $\gamma'' + 2$. The results, together with the corresponding correlation coefficients r' and r'' , respectively, are shown in the lower rows of Fig. 18. The three linear regressions give almost indistinguishable results for the exponents γ , γ' , and γ'' , and, for each energy E , at least one of the three correlation coefficients r , r' , or r'' is close to 1. For instance, the coefficient $|r''|$ has values away from 1 for $E \gtrsim 6.45E_r$ since the slope $\gamma'' + 2$ for $\ln[\overline{P^{-1}} \cdot (L/a)^2]$ is about 0. It is, however, close to 1 for low-energy states, and the scaling given by γ'' (essentially equal to γ and γ') is reliable in this regime. In general, the fitted slope γ yields the correct scaling and the quality is assessed by either r , r' , or r'' .

So far, we have not discussed the spread of IPR values in a given energy window. For extended and localized domains, we find that this will not greatly influence our results. To show this, we plot in Fig. 19 histograms of IPR occurrences for different system sizes, for the same energy windows as in Fig. 4 for a localized state (upper row) and an extended state (lower row). The horizontal axis is rescaled as $P^{-1} \times L^{-\gamma}$ with $\gamma = 0$ (left column) or $\gamma = -2$ (right column). We find

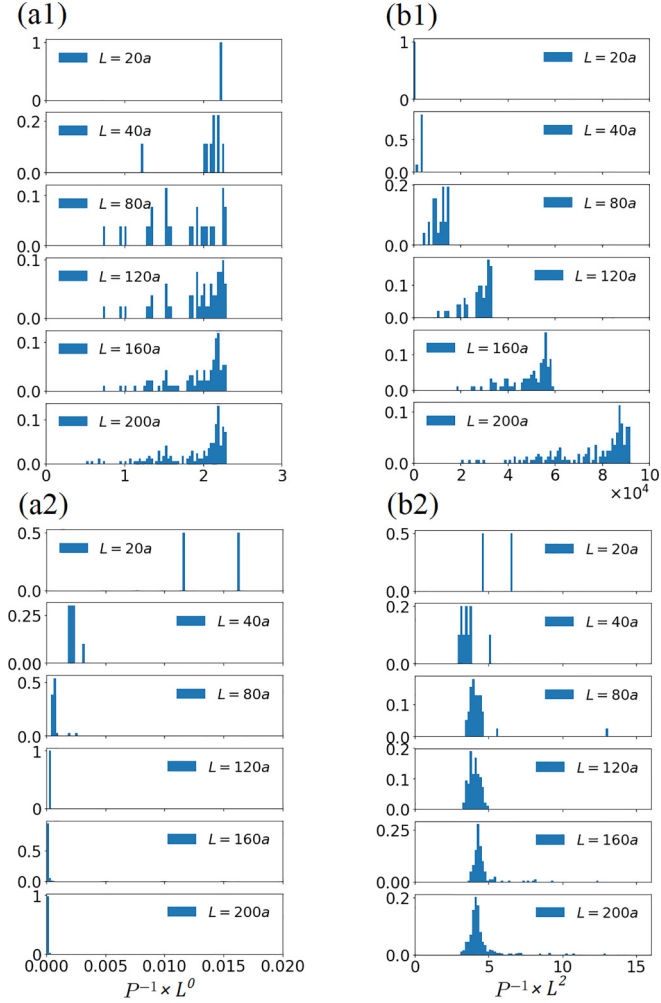


FIG. 19. Distributions of IPR for different system sizes L , where the horizontal axis is rescaled as $P^{-1} \times L^{-\gamma}$, with $\gamma = 0$ (left column) and -2 (right column), for energy windows (upper row) $E/E_r \in [4.00, 4.01]$ in the localized domain and (lower row) $E/E_r \in [6.45, 6.46]$ in the extended domain.

that the distributions are peaked, and remain fixed in position as a function of L for the correct choice of scaling ($\gamma = 0$ for the localized state and $\gamma = -2$ for the extended state). In contrast, for the opposite choice of the scaling, the position drifts. This immediately verifies that the underlying states are either localized or extended.

The behavior of critical states, however, is more complicated. In Fig. 20, we consider the critical energy window of Fig. 4. The spread of IPR values is much larger, which would of course inflate the relative error bars of the average IPR. However, we observe that the distribution clearly shows a single peak. Moreover, the distributions are shifted for both rescalings $\gamma = 0$ or -2 for increasing L . This indicates that a majority of states in the considered energy window are neither localized or extended, but critical.

APPENDIX C: STRUCTURES WITHIN CRITICAL STATES

The two kinds of critical states shown in Figs. 8 and 9 both have the ring states discussed in Sec. V as the building

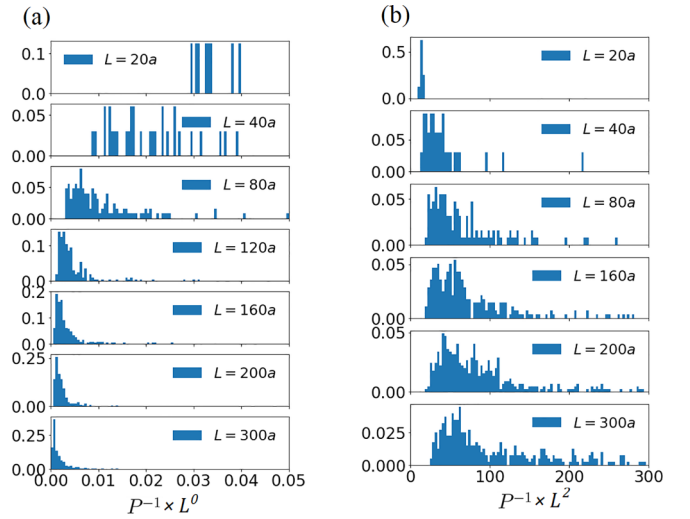


FIG. 20. Distributions of IPR for different system sizes L , where the horizontal axis is rescaled as $P^{-1} \times L^{-\gamma}$, with $\gamma = 0$ (left) and -2 (right), for energy windows $E/E_r \in [5.81, 5.82]$ in the critical domain.

blocks. The ring-shaped critical states shown in Fig. 8 have the ring states with winding $m = 0$ as the building blocks [see Figs. 11(a1) and 11(b1)]; note that these critical states have energy slightly smaller than Figs. 11(a1) and 11(b1). The building blocks of square-shaped critical states shown in Fig. 9 are the ring states with winding number $m = 2$ [see Figs. 11(a4), 11(b4), 11(a5), and 11(b5)], and these critical states have energy slightly larger than Figs. 11(a4), 11(b4), 11(a5), and 11(b5). As we discussed in Sec. V, the off-centered ring states have lower energy than the centered one for $m = 0$ and higher energy than the centered

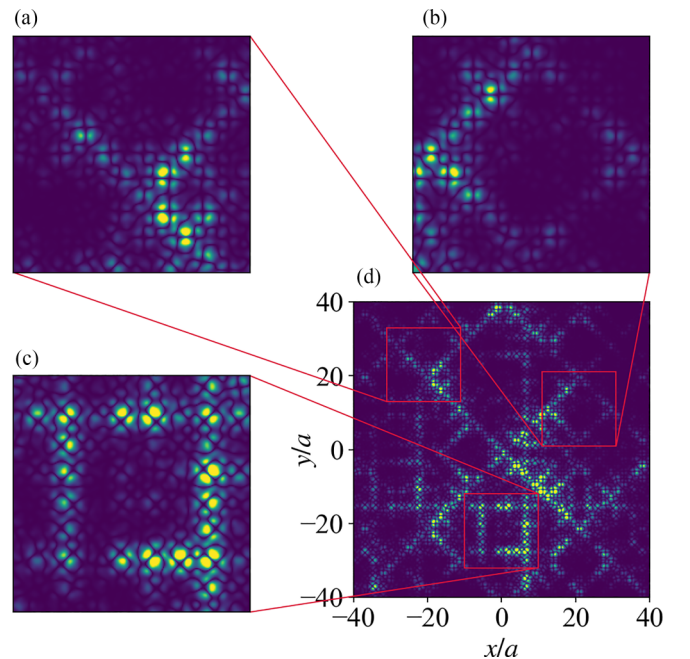


FIG. 21. (a)–(c) Zoomed up plots of several regions of the wave function shown in (d), which is a copy of Fig. 9(d).

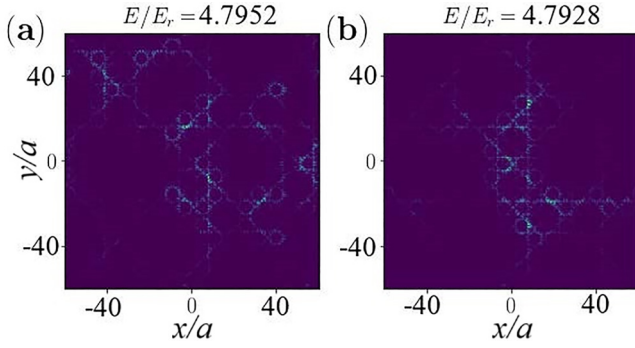


FIG. 22. Examples of critical states with energy near $E \simeq 4.8E_r$, which are composed of $m = 1$ ring state components (i.e., a single node line). We consider $V_0 = 2.5E_r$ and $L/a = 100$. Localized components become coupled in circular, ringlike arrangements. These circular structures are then coupled across diagonal lines.

one for $m = 2$. At a certain point, off-centered ring states at different locations hybridize together, forming the critical states.

The square shape of the critical states in Fig. 9 can be understood from the shape of the $m = 2$ ring states, as shown in Figs. 11(a4), 11(b4), 11(a5), and 11(b5). They may have node lines in diagonal directions as Figs. 11(a4) and 11(b4) or in horizontal and vertical directions as Figs. 11(a5) and 11(b5). When these $m = 2$ ring states couple to each other, they tend to connect in the direction where the bright spots touch, as this will give a strong coupling. As a result, $m = 2$ ring states with node lines in diagonal directions couple to each other along horizontal and vertical directions, and ring states with node lines in horizontal and vertical directions couple to each other along diagonal directions. Figure 21 shows several regions of the wave function Fig. 9(d), plotted in zoomed up scales. We can see that the typical directions of the state structure are indeed different from the directions of the node lines in each of the unit spots.

Finally, in Fig. 22, we show two examples of critical states with energy near $E \simeq 4.8E_r$. These states are composed of hybridized ringlike structures on small scale, with a similar square-shaped pattern to what has been observed before on large scale. At the intermediate length scale, we observe cir-

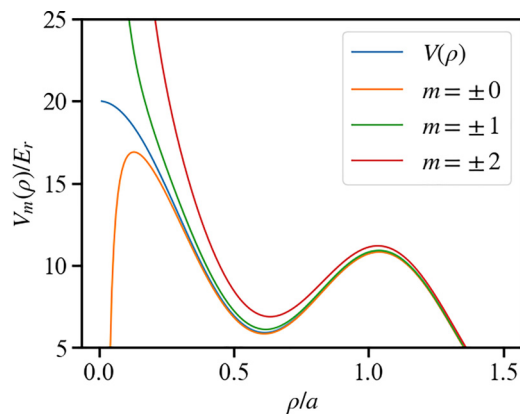


FIG. 23. Effective potential $V_m(\rho)$ for a quasicrystal potential with amplitude $V_0 = 5E_r$ and for various winding numbers m .

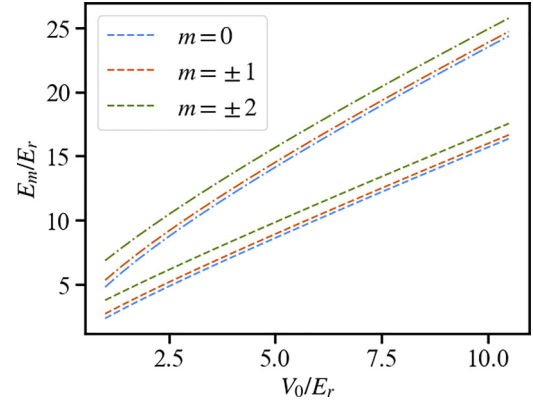


FIG. 24. Eigenenergies of the centered ring states in the radial ground state ($n = 0$, dashed lines) and first excited state ($n = 1$, dotted-dashed lines) with winding numbers $m = 0$ (blue), ± 1 (red), and ± 2 (green).

cular structures composed of several ring states with a single node line each (i.e., $m = 1$ ring states). The node lines are aligned in such a way to face the center of the circle. Different circles couple together and form extensive critical states.

APPENDIX D: RING STATES AND WINDING NUMBER

We discuss here the main properties of the ring states.

1. Centered ring states

The centered ring states live in an annular potential valley centered on $\mathbf{r} = 0$ with radius ρ_0 . In the vicinity of the potential valley, the angular dependence of the potential is of the order of $0.025V_0$, much smaller than any typical energy scale in this system, leading to wave-function modulations less than 10% for $V_0 \lesssim 10E_r$. We can thus neglect it and write $V(\rho, \theta) \simeq V(\rho)$. Owing to rotation symmetry, the local Schrödinger equation and the planar angular momentum operator $\hat{L}_z = -i\hbar \frac{\partial}{\partial \theta}$ may be diagonalized simultaneously. The energy eigenstates read as $\phi(\rho, \theta) = u_m(\rho)e^{im\theta}$, with $m \in \mathbb{Z}$. Writing $u_m(\rho) = \rho^{-1/2}f_m(\rho)$, the amplitude $f_m(\rho)$ is then governed by the semi-infinite one-dimensional, radial equation

$$-\frac{\hbar^2}{2M} \frac{d^2}{d\rho^2} f_m(\rho) + V_m(\rho) f_m(\rho) = E_m f_m(\rho), \quad \rho > 0 \quad (\text{D1})$$

with the effective potential

$$V_m(\rho) = V(\rho) + \frac{\hbar^2}{2M} \frac{4m^2 - 1}{4\rho^2}. \quad (\text{D2})$$

The latter consists of the bare potential $V(\rho)$ and a centrifugal term.

As shown in Fig. 23, the centrifugal term strongly deforms the potential for $\rho \lesssim 0.1a$, but the distortion near the minimum, $\rho_0 \simeq 0.61a$, is weak enough that the radial eigenfunction $f_m(\rho)$ weakly depends on m for sufficiently large V_0 and small m . For a sufficiently deep potential well, we may use a harmonic approximation and write

$$V_m(\rho) \simeq V_m(\rho_0) + \frac{1}{2} M \omega_m^2 (\rho - \rho_0)^2. \quad (\text{D3})$$

$\Delta V/E_r$	$m = 0$	$m = +1$	$m = -1$	$m = -2$	$m = +2$	$m = -3$	$m = +3$
$m = 0$	0.01082852	0.00425186	0.00425186	0.03266841	0.03266841	0.12117409	0.12117409
$m = +1$		0.01138857	0.03902952	0.24707624	0.02948781	0.00013442	0.01177908
$m = -1$			0.01138857	0.02948781	0.24707624	0.01177908	0.00013442
$m = -2$				0.00954469	0.00070855	0.03857501	0.12243
$m = +2$					0.00954469	0.12243	0.03857501
$m = -3$						0.00321993	0.04628118
$m = +3$							0.00321993

FIG. 25. Perturbation matrix of the ring states.

The dependence of ω_m on m is less than 10% for $V_0 > 3E_r$ and $|m| \leq 2$, and we can omit the subscript. Similarly, the radius of the local minimum is almost independent of m in the same range of parameters. The extension of the radial ground-state wave function is given by $\Delta\rho = \sqrt{\langle(\rho - \rho_0)^2\rangle} \simeq \sqrt{\hbar/2M\omega}$. For $V_0 \gtrsim 3E_r$, it is small enough, $\Delta\rho \lesssim 0.2a$, that the harmonic approximation is good. As a result, the low-energy centered ring eigenstates have energies

$$E_{m,n} \simeq V(\rho_0) + \hbar\omega(n + 1/2) + \frac{\hbar^2}{2M} \frac{4m^2 - 1}{4\rho_0^2}, \quad (\text{D4})$$

where $n \in \mathbb{N}$ denotes the n th radial excited state. These eigenenergies are plotted in Fig. 24 for $n = 0$ and 1, and

$|m| \leq 2$. In the range of interest, we find that the lowest-energy states are, successively, $m = 0, \pm 1$, and ± 2 , all with $n = 0$. Hence, the radial excitations have a higher energy, and we may restrict to the $n = 0$ sector. The relevant ring state only differs by their orbital rotation energy, getting the theoretical estimate

$$E_m - E_0 = \frac{\hbar^2}{2M} \frac{m^2}{\rho_0^2}, \quad (\text{D5})$$

with $E_0 \simeq V(\rho_0) + \hbar\omega/2 - \hbar^2/8M\rho_0^2$. This is nothing but Eq. (6).

2. Perturbative coupling terms for off-centered ring states

Figure 25 shows, in units of E_r , the moduli of all the perturbation matrix elements $\langle\phi_{m_1}|\Delta V|\phi_{m_2}\rangle$ [see Eq. (7)] between the seven ring states with winding numbers $m = 0, \pm 1, \pm 2$, and ± 3 . The perturbation ΔV is the difference between the potentials around $\mathbf{r}_0 = (19.06a, 4.95a)$ and around $\mathbf{r} = 0$. Since the matrix is symmetric, only the upper half is shown. The numbers in red are the strongest couplings while those in black are at least about one order of magnitude smaller.

-
- [1] D. Shechtman, I. Blech, D. Gratias, and J. W. Cahn, Metallic phase with long-range orientational order and no translational symmetry, *Phys. Rev. Lett.* **53**, 1951 (1984).
- [2] D. Levine and P. J. Steinhardt, Quasicrystals: A new class of ordered structures, *Phys. Rev. Lett.* **53**, 2477 (1984).
- [3] M. Senechal, *Quasicrystals and Geometry* (Cambridge University Press, Cambridge, UK, 1995).
- [4] Z. M. Stadnik, *Physical Properties of Quasicrystals*, Vol. 126 (Springer, Berlin, 1998).
- [5] W. Steurer, Twenty years of structure research on quasicrystals. Part I. Pentagonal, octagonal, decagonal and dodecagonal quasicrystals, *Z. Kristallogr. Crystallogr. Mater.* **219**, 391 (2004).
- [6] J.-B. Suck, M. Schreiber, and P. Häussler, *Quasicrystals: An Introduction to Structure, Physical Properties and Applications*, Vol. 55 (Springer, Berlin, 2013).
- [7] W. Steurer, Quasicrystals: What do we know? What do we want to know? What can we know? *Acta Crystallogr., Sect. A: Found. Adv.* **74**, 1 (2018).
- [8] D. Shechtman and I. A. Blech, The microstructure of rapidly solidified Al_6Mn , *Metall. Trans. A* **16**, 1005 (1985).
- [9] L. Bindi, J. M. Eiler, Y. Guan, L. S. Hollister, G. MacPherson, P. J. Steinhardt, and N. Yao, Evidence for the extraterrestrial origin of a natural quasicrystal, *Proc. Natl. Acad. Sci. USA* **109**, 1396 (2012).
- [10] L. Bindi, N. Yao, C. Lin, L. S. Hollister, C. L. Andronicos, V. V. Distler, M. P. Eddy, A. Kostin, V. Kryachko, G. J. MacPherson *et al.*, Natural quasicrystal with decagonal symmetry, *Sci. Rep.* **5**, 1 (2015).
- [11] L. Bindi, W. Kolb, G. N. Eby, P. D. Asimow, T. C. Wallace, and P. J. Steinhardt, Accidental synthesis of a previously unknown quasicrystal in the first atomic bomb test, *Proc. Natl. Acad. Sci. USA* **118**, e2101350118 (2021).
- [12] S. Walter and S. Deloudi, *Crystallography of Quasicrystals: Concepts, Methods and Structures*, Vol. 126 (Springer, Berlin, 2009).
- [13] S. Schmid, R. L. Withers, and R. Lifshitz, *Aperiodic Crystals* (Springer, Berlin, 2013).
- [14] L. Landau and E. Lifshitz, *Statistical Physics (Course of Theoretical Physics Vol. 5), 1st ed.* (Addison-Wesley, Boston, 1958).
- [15] C. Kittel, P. McEuen, and P. McEuen, *Introduction to Solid State Physics*, Vol. 8 (Wiley New York, 1996).
- [16] M. Senechal, *Crystalline Symmetries: An Informal Mathematical Introduction* (CRC Press, Boca Raton, FL, 1990).
- [17] A. L. Mackay, Crystallography and the Penrose pattern, *Phys. A (Amsterdam)* **114**, 609 (1982).
- [18] A. L. Mackay, De nive quinquangula: On the pentagon snowflake, *Kristallografiya* **26**, 910 (1981) [*Sov. Phys.–Crystallogr.* **26**, 517 (1981)].
- [19] K. Edagawa, K. Suzuki, and S. Takeuchi, High resolution transmission electron microscopy observation of thermally fluctuating phasons in decagonal Al-Cu-Co , *Phys. Rev. Lett.* **85**, 1674 (2000).
- [20] J. E. S. Socolar, T. C. Lubensky, and P. J. Steinhardt, Phonons, phasons, and dislocations in quasicrystals, *Phys. Rev. B* **34**, 3345 (1986).
- [21] P. A. Bancel, Dynamical phasons in a perfect quasicrystal, *Phys. Rev. Lett.* **63**, 2741 (1989).
- [22] K. Kamiya, T. Takeuchi, N. Kabeya, N. Wada, T. Ishimasa, A. Ochiai, K. Deguchi, K. Imura, and N. Sato,

- Discovery of superconductivity in quasicrystal, *Nat. Commun.* **9**, 1 (2018).
- [23] S. Poon, Electronic properties of quasicrystals an experimental review, *Adv. Phys.* **41**, 303 (1992).
- [24] D. Mayou, C. Berger, F. Cyrot-Lackmann, T. Klein, and P. Lanco, Evidence for unconventional electronic transport in quasicrystals, *Phys. Rev. Lett.* **70**, 3915 (1993).
- [25] S. J. Ahn, P. Moon, T.-H. Kim, H.-W. Kim, H.-C. Shin, E. H. Kim, H. W. Cha, S.-J. Kahng, P. Kim, M. Koshino *et al.*, Dirac electrons in a dodecagonal graphene quasicrystal, *Science* **361**, 782 (2018).
- [26] W. Yao, E. Wang, C. Bao, Y. Zhang, K. Zhang, K. Bao, C. K. Chan, C. Chen, J. Avila, M. C. Asensio *et al.*, Quasicrystalline 30° twisted bilayer graphene as an incommensurate superlattice with strong interlayer coupling, *Proc. Natl. Acad. Sci. USA* **115**, 6928 (2018).
- [27] T. S. Cubitt, D. Perez-Garcia, and M. M. Wolf, Undecidability of the spectral gap, *Nature (London)* **528**, 207 (2015).
- [28] T. Fujiwara, S. Yamamoto, and G. Trambly de Laissardière, Band structure effects of transport properties in icosahedral quasicrystals, *Phys. Rev. Lett.* **71**, 4166 (1993).
- [29] T. Odagaki and D. Nguyen, Electronic and vibrational spectra of two-dimensional quasicrystals, *Phys. Rev. B* **33**, 2184 (1986).
- [30] I. Buluta and F. Nori, Quantum simulators, *Science* **326** (5949), 108 (2009).
- [31] J. I. Cirac and P. Zoller, Goals and opportunities in quantum simulation, *Nat. Phys.* **8**, 264 (2012); I. Bloch, J. Dalibard, and S. Nascimbène, Quantum simulations with ultracold quantum gases, *ibid.* **8**, 267 (2012); R. Blatt and C. F. Roos, Quantum simulations with trapped ions, *ibid.* **8**, 277 (2012); A. Aspuru-Guzik and P. Walther, Photonic quantum simulators, *ibid.* **8**, 285 (2012); A. A. Houck, H. E. Tureci, and J. Koch, On-chip quantum simulation with superconducting circuits, *ibid.* **8**, 292 (2012).
- [32] C. Gross and I. Bloch, Quantum simulations with ultracold atoms in optical lattices, *Science* **357**, 995 (2017).
- [33] L. Sanchez-Palencia, Quantum simulation: From basic principles to applications, *C. R. Phys.* **19**, 357 (2018); L. Tarruell and L. Sanchez-Palencia, Quantum simulation of the Hubbard model with ultracold fermions in optical lattices, *ibid.* **19**, 365 (2018); M. Aidelsburger, S. Nascimbene, and N. Goldman, Artificial gauge fields in materials and engineered systems, *ibid.* **19**, 394 (2018); J. Lebreuilly and I. Carusotto, Quantum simulation of zero temperature quantum phases and incompressible states of light via non-Markovian reservoir engineering techniques, *ibid.* **19**, 433 (2018); K. Le Hur, L. Henriot, L. Herviou, K. Plekhanov, A. Petrescu, T. Goren, M. Schiro, C. Mora, and P. P. Orth, Driven dissipative dynamics and topology of quantum impurity systems, *ibid.* **19**, 451 (2018); M. Bell, B. Douçot, M. Gershenson, L. Ioffe, and A. Petkovic, Josephson ladders as a model system for 1D quantum phase transitions, *ibid.* **19**, 484 (2018); F. Alet and N. Laflorencie, Many-body localization: An introduction and selected topics, *ibid.* **19**, 498 (2018).
- [34] Y. S. Chan, C. T. Chan, and Z. Y. Liu, Photonic band gaps in two dimensional photonic quasicrystals, *Phys. Rev. Lett.* **80**, 956 (1998).
- [35] Y. Lahini, R. Pugatch, F. Pozzi, M. Sorel, R. Morandotti, N. Davidson, and Y. Silberberg, Observation of a localization transition in quasiperiodic photonic lattices, *Phys. Rev. Lett.* **103**, 013901 (2009).
- [36] B. Freedman, G. Bartal, M. Segev, R. Lifshitz, D. N. Christodoulides, and J. W. Fleischer, Wave and defect dynamics in nonlinear photonic quasicrystals, *Nature (London)* **440**, 1166 (2006).
- [37] Z. V. Vardeny, A. Nahata, and A. Agrawal, Optics of photonic quasicrystals, *Nat. Photonics* **7**, 177 (2013).
- [38] D. Tanese, E. Gurevich, F. Baboux, T. Jacqmin, A. Lemaître, E. Galopin, I. Sagnes, A. Amo, J. Bloch, and E. Akkermans, Fractal energy spectrum of a polariton gas in a Fibonacci quasiperiodic potential, *Phys. Rev. Lett.* **112**, 146404 (2014).
- [39] F. Baboux, E. Levy, A. Lemaître, C. Gómez, E. Galopin, L. Le Gratiet, I. Sagnes, A. Amo, J. Bloch, and E. Akkermans, Measuring topological invariants from generalized edge states in polaritonic quasicrystals, *Phys. Rev. B* **95**, 161114 (2017).
- [40] V. Goblot, A. Strkalj, N. Pernet, J. L. Lado, C. Dorow, A. Lemaître, L. L. Gratiet, A. Harouri, I. Sagnes, S. Ravets *et al.*, Emergence of criticality through a cascade of delocalization transitions in quasiperiodic chains, *Nat. Phys.* **16**, 832 (2020).
- [41] L. Sanchez-Palencia and L. Santos, Bose-Einstein condensates in optical quasicrystal lattices, *Phys. Rev. A* **72**, 053607 (2005).
- [42] K. Viebahn, M. Sbroscia, E. Carter, J.-C. Yu, and U. Schneider, Matter-wave diffraction from a quasicrystalline optical lattice, *Phys. Rev. Lett.* **122**, 110404 (2019).
- [43] M. Lewenstein, A. Sanpera, V. Ahufinger, B. Damski, A. Sen, and U. Sen, Ultracold atomic gases in optical lattices: Mimicking condensed matter physics and beyond, *Adv. Phys.* **56**, 243 (2007).
- [44] I. Bloch, J. Dalibard, and W. Zwerger, Many-body physics with ultracold gases, *Rev. Mod. Phys.* **80**, 885 (2008).
- [45] C. Chin, R. Grimm, P. Julienne, and E. Tiesinga, Feshbach resonances in ultracold gases, *Rev. Mod. Phys.* **82**, 1225 (2010).
- [46] L. Sanchez-Palencia and M. Lewenstein, Disordered quantum gases under control, *Nat. Phys.* **6**, 87 (2010).
- [47] G. Modugno, Anderson localization in Bose-Einstein condensates, *Rep. Prog. Phys.* **73**, 102401 (2010).
- [48] N. Macé, A. Jagannathan, and M. Duneau, Quantum simulation of a 2D quasicrystal with cold atoms, *Crystals* **6**, 124 (2016).
- [49] R. Roth and K. Burnett, Phase diagram of bosonic atoms in two-color superlattices, *Phys. Rev. A* **68**, 023604 (2003).
- [50] B. Damski, J. Zakrzewski, L. Santos, P. Zoller, and M. Lewenstein, Atomic Bose and Anderson glasses in optical lattices, *Phys. Rev. Lett.* **91**, 080403 (2003).
- [51] G. Roati, C. D'Errico, L. Fallani, M. Fattori, C. Fort, M. Zaccanti, G. Modugno, M. Modugno, and M. Inguscio, Anderson localization of a non-interacting Bose-Einstein condensate, *Nature (London)* **453**, 895 (2008).
- [52] L. Fallani, J. E. Lye, V. Guarrera, C. Fort, and M. Inguscio, Ultracold atoms in a disordered crystal of light: Towards a Bose glass, *Phys. Rev. Lett.* **98**, 130404 (2007).
- [53] T. Roscilde, Bosons in one-dimensional incommensurate superlattices, *Phys. Rev. A* **77**, 063605 (2008).
- [54] G. Roux, T. Barthel, I. P. McCulloch, C. Kollath, U. Schollwöck, and T. Giamarchi, Quasiperiodic Bose-Hubbard model and localization in one-dimensional cold atomic gases, *Phys. Rev. A* **78**, 023628 (2008).

- [55] B. Gadway, D. Pertot, J. Reeves, M. Vogt, and D. Schneble, Glassy behavior in a binary atomic mixture, *Phys. Rev. Lett.* **107**, 145306 (2011).
- [56] C. D'Errico, E. Lucioni, L. Tanzi, L. Gori, G. Roux, I. P. McCulloch, T. Giamarchi, M. Inguscio, and G. Modugno, Observation of a disordered bosonic insulator from weak to strong interactions, *Phys. Rev. Lett.* **113**, 095301 (2014).
- [57] L. Gori, T. Barthel, A. Kumar, E. Lucioni, L. Tanzi, M. Inguscio, G. Modugno, T. Giamarchi, C. D'Errico, and G. Roux, Finite-temperature effects on interacting bosonic one-dimensional systems in disordered lattices, *Phys. Rev. A* **93**, 033650 (2016).
- [58] F. A. An, E. J. Meier, and B. Gadway, Engineering a flux-dependent mobility edge in disordered zigzag chains, *Phys. Rev. X* **8**, 031045 (2018).
- [59] F. A. An, K. Padavić, E. J. Meier, S. Hegde, S. Ganeshan, J. H. Pixley, S. Vishveshwara, and B. Gadway, Interactions and mobility edges: Observing the generalized Aubry-André model, *Phys. Rev. Lett.* **126**, 040603 (2021).
- [60] H. Yao, H. Khoudli, L. Bresque, and L. Sanchez-Palencia, Critical behavior and fractality in shallow one-dimensional quasiperiodic potentials, *Phys. Rev. Lett.* **123**, 070405 (2019).
- [61] H. Yao, T. Giamarchi, and L. Sanchez-Palencia, Lieb-Liniger bosons in a shallow quasiperiodic potential: Bose glass phase and fractal Mott lobes, *Phys. Rev. Lett.* **125**, 060401 (2020).
- [62] S. Lellouch and L. Sanchez-Palencia, Localization transition in weakly-interacting Bose superfluids in one-dimensional quasiperiodic lattices, *Phys. Rev. A* **90**, 061602(R) (2014).
- [63] S. Iyer, V. Oganesyan, G. Refael, and D. A. Huse, Many-body localization in a quasiperiodic system, *Phys. Rev. B* **87**, 134202 (2013).
- [64] M. Schreiber, S. S. Hodgman, P. Bordia, H. P. Lüschen, M. H. Fischer, R. Vosk, E. Altman, U. Schneider, and I. Bloch, Observation of many-body localization of interacting fermions in a quasi-random optical lattice, *Science* **349**, 842 (2015).
- [65] V. Khemani, D. N. Sheng, and D. A. Huse, Two universality classes for the many-body localization transition, *Phys. Rev. Lett.* **119**, 075702 (2017).
- [66] T. Kohlert, S. Scherg, X. Li, H. P. Lüschen, S. Das Sarma, I. Bloch, and M. Aidelsburger, Observation of many-body localization in a one-dimensional system with a single-particle mobility edge, *Phys. Rev. Lett.* **122**, 170403 (2019).
- [67] T. Liu, X. Xia, S. Longhi, and L. Sanchez-Palencia, Anomalous mobility edges in one-dimensional quasiperiodic models, *SciPost Phys.* **12**, 027 (2022).
- [68] A. Szabó and U. Schneider, Mixed spectra and partially extended states in a two-dimensional quasiperiodic model, *Phys. Rev. B* **101**, 014205 (2020).
- [69] M. Sbroscia, K. Viebahn, E. Carter, J.-C. Yu, A. Gaunt, and U. Schneider, Observing localization in a 2D quasicrystalline optical lattice, *Phys. Rev. Lett.* **125**, 200604 (2020).
- [70] D. Johnstone, P. Öhberg, and C. W. Duncan, Mean-field phases of an ultracold gas in a quasicrystalline potential, *Phys. Rev. A* **100**, 053609 (2019).
- [71] D. Johnstone, P. Öhberg, and C. W. Duncan, The mean-field Bose glass in quasicrystalline systems, *J. Phys. A: Math. Theor.* **54**, 395001 (2021).
- [72] R. Gautier, H. Yao, and L. Sanchez-Palencia, Strongly interacting bosons in a two-dimensional quasicrystal lattice, *Phys. Rev. Lett.* **126**, 110401 (2021).
- [73] M. Ciardi, T. Macrì, and F. Cinti, Finite-temperature phases of trapped bosons in a two-dimensional quasiperiodic potential, *Phys. Rev. A* **105**, L011301 (2022).
- [74] Z. Zhu, H. Yao, and L. Sanchez-Palencia, Thermodynamic phase diagram of two-dimensional bosons in a quasicrystal potential, *Phys. Rev. Lett.* **130**, 220402 (2023).
- [75] E. Gottlob and U. Schneider, Hubbard models for quasicrystalline potentials, *Phys. Rev. B* **107**, 144202 (2023).
- [76] J.-C. Yu, S. Bhave, L. Reeve, B. Song, and U. Schneider, Observing the two-dimensional Bose glass in an optical quasicrystal, [arXiv:2303.00737](https://arxiv.org/abs/2303.00737).
- [77] S. Aubry and G. André, Analyticity breaking and Anderson localization in incommensurate lattices, *Ann. Isr. Phys. Soc.* **3**, 133 (1980).
- [78] P. W. Anderson, Absence of diffusion in certain random lattices, *Phys. Rev.* **109**, 1492 (1958).
- [79] J. Biddle, B. Wang, D. J. Priour Jr, and S. Das Sarma, Localization in one-dimensional incommensurate lattices beyond the Aubry-André model, *Phys. Rev. A* **80**, 021603 (2009).
- [80] A. Saul, A. M. Llois, and M. Weissmann, Wavefunctions of one-dimensional incommensurate hamiltonians: The fractal dimension and its relationship with localisation, *J. Phys. C: Solid State Phys.* **21**, 2137 (1988).
- [81] H. Hiramoto and M. Kohmoto, Scaling analysis of quasiperiodic systems: Generalized Harper model, *Phys. Rev. B* **40**, 8225 (1989).
- [82] M. N. Kosch, L. Asteria, H. P. Zahn, K. Sengstock, and C. Weitenberg, Multifrequency optical lattice for dynamic lattice-geometry control, *Phys. Rev. Res.* **4**, 043083 (2022).
- [83] S. E. Pollack, D. Dries, M. Junker, Y. P. Chen, T. A. Corcovilos, and R. G. Hulet, Extreme tunability of interactions in a ⁷Li Bose-Einstein condensate, *Phys. Rev. Lett.* **102**, 090402 (2009).
- [84] L. Sanchez-Palencia, D. Clément, P. Lugan, P. Bouyer, G. V. Shlyapnikov, and A. Aspect, Anderson localization of expanding Bose-Einstein condensates in random potentials, *Phys. Rev. Lett.* **98**, 210401 (2007).
- [85] J. Billy, V. Josse, Z. Zuo, A. Bernard, B. Hambrecht, P. Lugan, D. Clément, L. Sanchez-Palencia, P. Bouyer, and A. Aspect, Direct observation of Anderson localization of matter waves in a controlled disorder, *Nature (London)* **453**, 891 (2008).
- [86] S. S. Kondov, W. R. McGehee, J. J. Zirbel, and B. DeMarco, Three-dimensional Anderson localization of ultracold fermionic matter, *Science* **334**, 66 (2011).
- [87] F. Jendrzejewski, A. Bernard, K. Müller, P. Cheinet, V. Josse, M. Piraud, L. Pezzé, L. Sanchez-Palencia, A. Aspect, and P. Bouyer, Three-dimensional localization of ultracold atoms in an optical disordered potential, *Nat. Phys.* **8**, 398 (2012).
- [88] R. C. Kuhn, O. Sigwarth, C. Miniatura, D. Delande, and C. A. Müller, Coherent matter wave transport in speckle potentials, *New J. Phys.* **9**, 161 (2007).

- [89] S. E. Skipetrov, A. Minguzzi, B. A. van Tiggelen, and B. Shapiro, Anderson localization of a Bose-Einstein condensate in a 3D random potential, *Phys. Rev. Lett.* **100**, 165301 (2008).
- [90] M. Piraud, P. Lugan, P. Bouyer, A. Aspect, and L. Sanchez-Palencia, Localization of a matter wave packet in a disordered potential, *Phys. Rev. A* **83**, 031603(R) (2011).
- [91] M. Piraud, L. Pezzé, and L. Sanchez-Palencia, Matter wave transport and Anderson localization in anisotropic three-dimensional disorder, *Europhys. Lett.* **99**, 50003 (2012).
- [92] M. Piraud, L. Pezzé, and L. Sanchez-Palencia, Quantum transport of atomic matter waves in anisotropic two-dimensional and three-dimensional disorder, *New J. Phys.* **15**, 075007 (2013).
- [93] L. Pezzé and L. Sanchez-Palencia, Localized and extended states in a disordered trap, *Phys. Rev. Lett.* **106**, 040601 (2011).